A comprehensive evaluation of the use of Lagrangian particle dispersion models for inverse modeling of greenhouse gas emissions

Martin Vojta[1], Andreas Plach[1,2], Rona L. Thompson[3], and Andreas Stohl[1]

[1]Department of Meteorology and Geophysics, University of Vienna, Vienna, Austria
[2]Physics Institute, Climate and Environmental Physics, University of Bern, Bern, Switzerland
[3]Norwegian Institute for Air Research NILU, Kjeller, Norway

Correspondence: Martin Vojta (martin.vojta@univie.ac.at)

Abstract. Using the example of sulfur hexafluoride (SF_6) we investigate the use of Lagrangian Particle Dispersion Models (LPDMs) for inverse modeling of greenhouse gas (GHG) emissions and explore the limitations of this approach. We put the main focus on the impacts of baseline methods and the LPDM backward simulation period on the *a posteriori* emissions determined by the inversion. We consider baseline methods that are based on a statistical selection of observations at individual

5   measurement sites and a global distribution based (GDB) approach, where global mixing ratio fields are coupled to the LPDM back-trajectories at their termination points. We show that purely statistical baseline methods cause large systematical errors, which lead to inversion results that are highly sensitive to the LPDM backward simulation period and can generate unrealistic global total *a posteriori* emissions. The GDB method produces *a posteriori* emissions that are far less sensitive to the backward simulation period and that are consistent with recognized global total emissions. Our results show that longer backward

10   simulation periods, beyond the often used 5 to 10 days, reduce the mean squared error and increase the correlation between *a priori* modeled and observed mixing ratios. Also, the inversion becomes less sensitive to biases in the *a priori* emissions and the global mixing ratio fields for longer backward simulation periods. Further, longer periods help to better constrain emissions in regions poorly covered by the global SF_6 monitoring network (e.g., Africa, South America). We find that the inclusion of existing flask measurements in the inversion helps to further close these gaps and suggest that a few additional and well placed

15   flask sampling sites would have great value for improving global *a posteriori* emission fields.

1 Introduction

Over the last few decades, the sharp increase of anthropogenic greenhouse gas (GHG) emissions has become a global concern, as it affects the Earth's climate with possible dangerous consequences for human health, infrastructure and ecosystems (IPCC, 2018). In order to prevent dangerous human interference with the climate system, the United Nations Framework Convention on

20   Climate Change (UNFCCC) was established. As an important commitment to the convention, Annex-I countries (industrialized nations that are legally bound to reduce GHG emissions) are required to report their national emissions for regulated GHGs. These inventories are compiled by applying "bottom-up" methods, where statistical economic production or consumption data and source-specific emission factors are used to estimate country emissions. However, "bottom-up" estimates are suspected to suffer from significant uncertainties and there is a growing need for independent verification of these estimates (e.g. Rypdal

25 et al., 2005; Weiss et al., 2021). Independent verification can be provided by "top-down" methods, such as inverse modeling (Henne et al., 2016).

Inverse modeling requires the use of atmospheric transport models, either Eulerian models or Lagrangian Particle Dispersion Models (LPDMs). LPDMs are usually run backward in time. They release a large number of virtual particles from a given observation location and time, and trace them backward for a limited simulation period. The model output gives the sensitivity

30 of the atmospheric mixing ratio to emissions during the backtracking time. In the inversion algorithm, the sensitivities for a large number of observations are used to optimize *a priori* emission estimates such that (with the obtained *a posteriori* emissions) the simulated mixing ratios better fit the atmospheric observations. Most studies only use *in situ* observations for this purpose, however low frequent flask measurements can also be included (e.g. Villani et al., 2010).

Previous studies argue that inversion methods have insufficient accuracy (e.g. Rypdal et al., 2005) and problems with repro-

35 ducibility (Berchet et al., 2021). In order to enhance the credibility of inverse modeling, a better knowledge of the associated uncertainties is required (Brunner et al., 2017). An important source of uncertainty regarding LPDM-based inversion methods is the fact that they are run backward in time only for a few days, e.g., 5 days (Brunner et al., 2017; Keller et al., 2012; Zhao et al., 2009), 10 days (Rigby et al., 2019; Schoenenberger et al., 2018; Simmonds et al., 2018) or 20 days (Fang et al., 2014; Maione et al., 2014; Stohl et al., 2009). The choices made by different authors seem arbitrary, and a systematic analysis of the

40 impact of the backward simulation period is lacking.

The inversions can only account for the emissions that have occurred during the backward simulation period. By contrast, the emission contributions prior to the limited LPDM backward simulation period are not explicitly modeled but must still be accounted for in order to compare the model results with the observations. These contributions must be collected in a so-called baseline that is added to the modeled contributions. As errors in the baseline translate to errors in the *a posteriori* emissions,

45 the baseline needs to be as accurate as possible. Many different methods have been suggested to determine this baseline.

Investigating halocarbons or fluorinated gases (F-gases) most studies use statistical methods to calculate the baseline by selecting low mixing ratio observations at individual stations (e.g. Ganesan et al., 2014; Prinn et al., 2000; Saito et al., 2010; Zeng et al., 2012). The general idea is to statistically identify observations which are assumed to be unaffected by emissions within the LPDM simulation period. A widely used statistical method is the robust estimation of baseline signal (REBS) method, in-

50 troduced by Ruckstuhl et al. (2012) which applies a robust local linear regression model. Statistical methods, however, always involve subjective data selection and treatment decisions, which can lead to problems. For instance, they will by definition wrongly classify measurements during longer lasting pollution episodes as baseline observations and therefore overestimate the baseline - a problem that is likely to occur frequently in polluted areas. It is also unclear to which degree these methods distinguish between lightly polluted air and measurement noise (Ryall et al., 2001). Furthermore, they fail to identify correct

55 baseline mixing ratios when they are below the lowest observations (Rigby et al., 2011), especially at polluted continental sites which virtually never receive air masses unaffected by emissions within the backward simulation period.

A baseline method introduced by Stohl et al. (2009), further termed as "Stohl's method", tries to avoid this baseline overestimation, by using model information to subtract prior simulated mixing ratios from pre-selected observations. Nevertheless, this pre-selection is subjective and prior simulated mixing ratios depend on *a priori* emission estimates.

60   Apart from using observations at each individual station to maintain a baseline, Rödenbeck et al. (2009) suggested a general "nesting" scheme, where a regional transport model – either a Eulerian or Lagrangian model – is embedded into a global model providing information from outside the spatio-temporal inversion domain. Such a global distribution based (GDB) approach was used by e.g. Trusilova et al. (2010) and Monteil and Scholze (2021) for carbon dioxide, and similar by Thompson and Stohl (2014) for methane. Whereas Rödenbeck et al. (2009) coupled the LPDM back-trajectories with the global model in

65   the space domain, Thompson and Stohl (2014) did the coupling at the time boundary. The GDB method defines the baseline exactly in the way it is needed for the inversion and can account for meteorological variability (i.e., transport of air from regions with lower or higher mixing ratios, respectively), which may cause sudden changes in the baseline. The accuracy of the GDB method, however, depends on how well the global field of mixing ratios can be modeled.

    The treatment of the baseline is critical when using LPDMs as a basis for atmospheric inversions. Still, it is unclear what

70   influence the choice of a certain baseline approach has on inversion results. Previous studies indicated that different approaches lead to significant mismatches in simulated emissions (Thompson and Stohl, 2014; Henne et al., 2016). However, different methods were never compared systematically and tested for different model set-ups such as the length of the LPDM backward simulations.

    Another problem of LPDM-based inversion studies is the general lack of consistency between regional emission estimates

75   and the global emissions of a GHG. Given that the LPDMs are usually run backward in time only for a few days, the inversions constrain the emissions only in regions where observation stations exist. This can lead to substantial deviations of the derived emissions from, often well known, global totals, a problem shared with regional inversion studies based on Eulerian models.

    In this study we [i] investigate the effect of the backward simulation time period within the range of 0-50 days, [ii] analyze the impact of the baseline definition on inversion results, [iii] examine their consistency with known global total emissions,

80   [iv] explore the influence of biases in the baseline and *a priori* emissions on inversion results for different backward simulation periods, and [v] compare the value of different observation types (flask vs. in-situ) for the inversion. We compare three different baseline methods - the REBS method, Stohl's method and the GDB method - and apply inverse modeling to the species sulfur hexafluoride (SF_6). SF_6 is the most potent GHG regulated under the Kyoto Protocol with a high global warming potential of approximately 23,500 over a 100-year time horizon (Myhre et al., 2013) and an estimated atmospheric lifetime of 3200 years

85   (Ravishankara et al., 1993). SF_6 is a convenient choice for our studies because it has no negative sources (as, e.g., CO_2), a very long lifetime in the atmosphere, well known global emissions, and there are relatively many measurements available. However, we expect our findings to also hold for other species and be informative for inverse modeling of GHGs with LPDMs in general.

2 Methods

2.1 Measurement data

90   The inversion (subsection 2.2) is performed by using atmospheric *in situ* observations of SF_6 dry-air mole fractions from 18 observation sites, distributed around the globe. Those measurements were provided by the Advanced Global Atmospheric Gases Experiment (AGAGE, Prinn et al., 2018) network, the NOAA/ESRL halocarbons *in situ* program (Dutton et al., 2017)

Table 1. Sites of surface *in situ* measurements used in the inversion and in the re-analysis.

Site ID	Station	Organisation	Calibration Scale	Latitude	Longitude	Altitude[a]	Frequency
CGO	Cape Grim, Tasmania	AGAGE	SIO-2005	40.7°S	144.7°E	94	2 hours
JFJ*	Jungfraujoch, Switzerland	AGAGE	SIO-2005	46.5°N	8.0°E	3580	2 hours
MHD	Mace Head, Ireland	AGAGE	SIO-2005	53.3°N	9.9°W	5	2 hours
RPB	Ragged Point, Barbados	AGAGE	SIO-2005	13.2°N	59.4°W	45	2 hours
SMO	Cape Matatula, American Samoa	AGAGE	SIO-2005	14.2°S	170.6°W	77	2 hours
THD	Trinidad Head, USA	AGAGE	SIO-2005	41.0°N	124.1°W	107	2 hours
ZEP	Zeppelin, Ny-Alesund, Norway	AGAGE	SIO-2005	78.9°N	11.9°E	474	2 hours
GSN	Gosan, South Korea	KNU/AGAGE	SIO-2005	33.3°N	126.2°E	89	2 hours
RGL	Ridge Hill, UK	UNIVBRIS	SIO-2005	52.0°N	2.5°W	204	30 min
ZSF*	Zugspitze-Schneefernerhaus, Germany	UBAG	WMO SF6 X2006	47.4°N	11.0°E	2671	1 hour
BRW	Barrow, Alaska, USA	NOAA	WMO SF6 X2014	71.3°N	156,6°E	11	1 hour
MLO*	Mauna Loa, USA	NOAA	WMO SF6 X2014	19.5°N	155.6°W	3397	1 hour
NWR*	Niwot Ridge, USA	NOAA	WMO SF6 X2014	40.0°N	105.6°W	3523	1 hour
SPO	South Pole, Antarctic	NOAA	WMO SF6 X2014	90.0°S	24.8°W	2841	1 hour
SUM	Summit, Greenland	NOAA	WMO SF6 X2014	72.6°N	38.5°W	3238	1 hour
IZO*	Izaña, Tenerife, Spain	AEMET	WMO SF6 X2014	28.3°N	16.5°W	2373	1 hour
COI	Cape Ochiishi, Japan	NIES	NIES-2008	43.2°N	145.5°E	49	1 hour
HAT	Hateruma, Japan	NIES	NIES-2008	24.1°N	123.8°E	47	1 hour

[a] The altitude specifies the sampling height in meters above sea level. Stations considered as mountain sites are marked with an asterisk.

and a number of independent organisations whose data were partly included in the World Data Centre for Greenhouse Gases (WDCGG, 2018). Measurement sites are listed in Table 1, together with acronyms and other station specific information.

95   At AGAGE stations, SF_6 mixing ratios are measured using Medusa Gas Chromatography followed by Mass Spectrometry (GC/MS, Miller et al., 2008). At the stations HAT and COI the SF_6 measurement system is based on cryogenic preconcentration and capillary GC/MS (Yokouchi et al., 2006). At all other stations, Gas Chromatography followed by Electron Capture Detection (GC-ECD) is used to measure SF_6 mole fractions. Observations were calibrated with four different SF_6 scales: SIO-2005, WMO SF6 X2006, WMO SF6 X2014 and NIES-2008. We converted all observations to the SIO-2005 calibration

100 scale, by dividing NIES-2008 calibrated data by the factor 1.013 (Saito, 2021) and WMO SF6 X2014 calibrated data by 1.002 (Guillevic et al., 2018). To convert mole fractions from WMO SF6 X2006 to WMO SF6 X2014, we used $y = ax^2 + bx + c$, where y corresponds to SF_6 mole fractions on the X2014 scale, x to mole fractions on the X2006 scale and the coefficients a, b, c have the values of $2.6821 \cdot 10^{-3}$, $9.7748 \cdot 10^{-1}$, and $3.5831 \cdot 10^{-2}$ (NOAA ESRL, 2014), respectively.

    We averaged all observation data over 3-hourly intervals. For stations at low altitudes, we selected afternoon values (12:00 to

105 16:00 local time), to only consider time periods with a well-mixed planetary boundary layer, when the smallest model errors can be expected. At mountain stations we instead selected observations during night times (00:00 to 04:00 local time) to avoid larger errors due to daytime small-scale up-slope winds in the complex topography around these sites, which are unresolved in the model. Additionally, we followed a method by Stohl et al. (2009) to remove observations that can not be brought into agreement
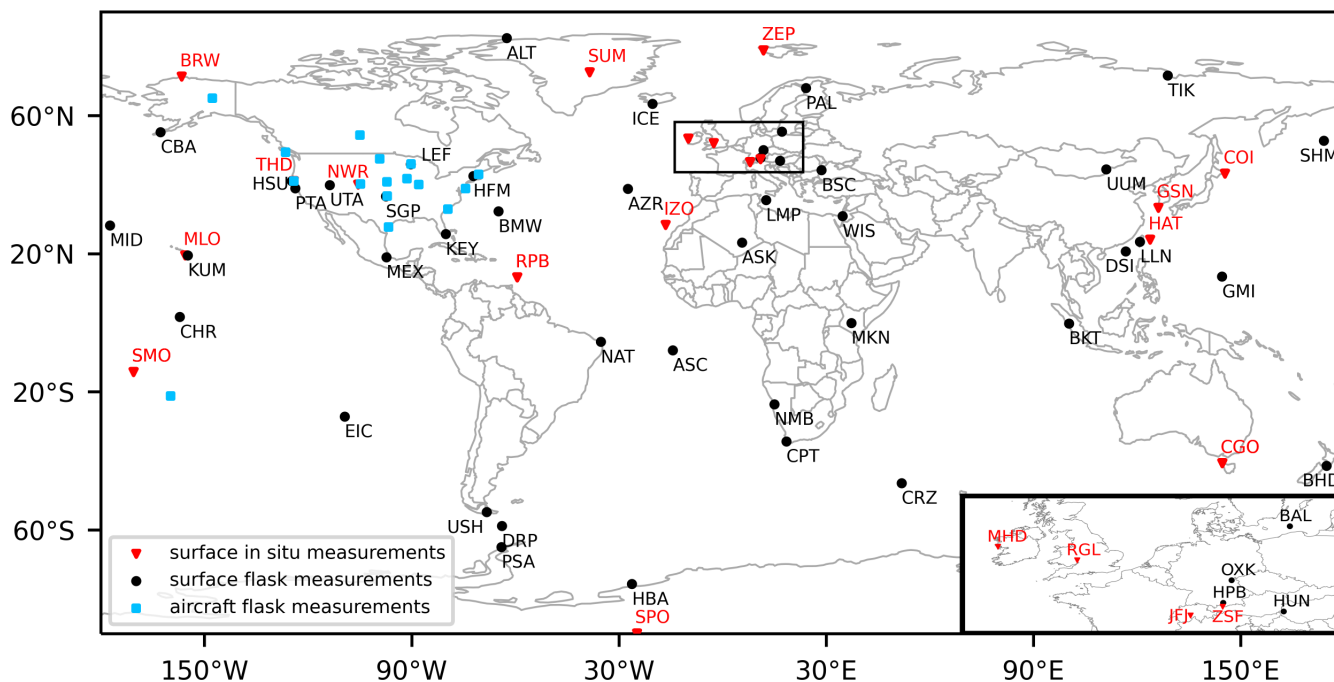
Figure 1. Map of surface *in situ* measurement sites used for the inversion (red triangles) and flask measurement sites (surface: black dots, aircraft: blue squares) that were additionally used for the re-analysis of SF$_6$

with modeled mixing ratios by the inversion. For this, we used the kurtosis of the *a posteriori* error frequency distribution and iteratively excluded observations causing the largest absolute errors until the kurtosis of the remaining error values fell below 5 (close to a Gaussian distribution). This method removed 0.62% (63 data points) of the whole dataset, affecting 0 to 2.92% of the observations at individual measurement sites. In total, 10,142 observations were used in the inversion for the year 2012.

For the re-analysis of SF$_6$ (see section 2.5) we used all the available 2011 and 2012 *in situ* measurements from the sites listed in Table 1. In addition, we included flask air samples from 44 surface observation stations (NOAA, Dlugokencky et al., 2020) and from 16 aircraft profiling stations (Sweeney et al., 2015; NOAA Carbon Cycle Group ObsPack Team, 2018). Surface flask measurements were available at intervals ranging from a few days up to months. Sampling flights were conducted irregularly with intervals between 2 and 5 weeks at individual sites. Aircraft measurements from individual flights provide vertical SF$_6$ mixing ratio profiles up to 8.5 km above sea level, where air samples are usually taken within less than an hour. With one exception, all aircraft samples were collected over North America. Additional information about the flask measurements from surface sites and aircraft programs can be found in Table A1 and Table A2 (Appendix). All flask measurements were calibrated with the WMO SF6 X2014 calibration scale and we converted them to the SIO-2005 calibration scale. For the re-analysis, we used 175,557 in-situ, 3,423 surface flask, and 5,581 aircraft measurements amounting to 184,561 measurements in total in 2011 and 2012. Fig. 1 provides an overview of all observation sites considered in the inversion and the re-analysis. In one

specific test case (see section 3.2) we also used the 2012 surface flask measurements in addition to the *in situ* measurments for
125 the inversion.

2.2 Inversion method

In this study we use the Bayesian inversion framework FLEXINVERT+ described in detail by Thompson and Stohl (2014),
which was further developed since then, to make the code more modular and to include iterative solution methods. However,
our results should be valid for all inversion methods based on LPDM calculations and we thus only include a brief description
130 of FLEXINVERT+. It is based on a linear forward operator $\mathbf{H}$ that represents the atmospheric transport, so that the forward
problem reads:

$$\mathbf{y} = \mathbf{H}\mathbf{x} + \varepsilon \tag{1}$$

where $\mathbf{y}$ is the vector of observed mixing ratios, $\mathbf{x}$ the emission state vector and ε the sum of observation and model error.
Since $\mathbf{H}$ is ill conditioned and has no unique inverse, *a priori* emission estimates can be added, in order to solve (1) for
135 $\mathbf{x}$. The inversion method applies Bayes' theorem to calculate *a posteriori* emissions, which on the one hand minimize the
difference between observed and modeled mixing ratios, and on the other hand stay close to the *a priori* emissions and inside
of predefined uncertainty bounds. Assumed uncertainties are Gaussian distributed resulting in a minimization of the cost
function (e.g. Tarantola, 2005).

$$\mathbf{J}(\mathbf{x}) = \frac{1}{2}(\mathbf{x} - \mathbf{x}_p)^T \mathbf{B}^{-1}(\mathbf{x} - \mathbf{x}_p) + \frac{1}{2}(\mathbf{H}\mathbf{x} - \mathbf{y})^T \mathbf{R}^{-1}(\mathbf{H}\mathbf{x} - \mathbf{y}) \tag{2}$$

140 where $\mathbf{B}$ is the *a priori* emission error covariance matrix, $\mathbf{R}$ the observation error covariance matrix, and $\mathbf{x}_p$ the vector of the *a
priori* emissions. This study uses the following analytical solution to minimize $\mathbf{J}(\mathbf{x})$:

$$\mathbf{x} = \mathbf{x}_p + (\mathbf{H}^T \mathbf{R}^{-1} \mathbf{H} + \mathbf{B}^{-1})^{-1} \mathbf{H}^T \mathbf{R}^{-1}(\mathbf{y} - \mathbf{H}\mathbf{x}) \tag{3}$$

We use a spatial emission grid (Fig. A1) with a varying grid size ranging from $1° \times 1°$ to $16° \times 16°$. We define the grid by
using model information to aggregate grid cells with low emission contributions, as further described by Thompson and Stohl
145 (2014). For this, the emission sensitivity is taken from the LPDM 50 day backward simulation and the resulting inversion grid
is used for all inversions. The output emission fields are saved at a spatial resolution of $1° \times 1°$.

SF$_6$ has no surface sinks and its surface fluxes can therefore only be larger or equal to zero. However, the inversion algorithm
can produce negative *a posteriori* fluxes. To overcome this problem we follow Thompson et al. (2015) and apply an inequality
constraint on the *a posteriori* emissions, using the truncated Gaussian approach by Thacker (2007). This approach, which
150 applies inequality constraints as error-free observations, is described by the following equation:

$$\hat{\mathbf{x}} = \mathbf{x} + \mathbf{A}\mathbf{P}^T(\mathbf{P}\mathbf{A}\mathbf{P}^T)^{-1}(\mathbf{c} - \mathbf{P}\mathbf{X}), \tag{4}$$

where $\mathbf{P}$ is a matrix operator selecting the fluxes violating the inequality constraint, and $\mathbf{c}$ a vector of the inequality constraint
(zero in our case). $\mathbf{x}$ and $\mathbf{A}$ represent the *a posteriori* emissions and error covariance matrix precalculated in the inversion,
respectively.

155   In contrast to many other studies (e.g., Henne et al., 2016; Stohl et al., 2009; Thompson and Stohl, 2014) we do not use the option to optimize the baseline mixing ratios in the inversion. This gives us the opportunity to better analyze the differences between investigated baseline methods and to study their impacts on the *a posteriori* emissions in detail.

2.3   Atmospheric transport

H is the so-called Source-Receptor-Relationship (SRR) in the context of atmospheric transport. The SRR is an emission
160   sensitivity that relates emission changes in a given grid cell to changes in modeled mixing ratios at a given receptor; for further details, see Seibert and Frank (2004). The SRR value in a specific grid cell (units of $1\frac{sm^3}{kg}$) measures the simulated mixing ratio change at a receptor that a unit strength source ($1\frac{kg}{sm^3}$) in that grid cell would create (Stohl et al., 2009).

In this study, we use the LPDM FLEXPART 10.4 (Pisso et al., 2019; Stohl et al., 1998, 2005) to calculate the SRR. The model is run in backward mode as this is more efficient than forward calculations when the number of emission grid cells
165   exceeds the number of observation sites. Available observations are averaged to three hourly means (see section 2.1). For each of these means 50,000 virtual particles are released continuously over the averaging period and followed backward in time. The SRR is calculated by determining the average time the particles spend in each grid cell of the $1°×1°$ output grid within the lowest 100 meters above the ground, assuming that all emissions occur at or near the ground. FLEXPART is driven by the hourly reanalysis dataset ERA5 (Hersbach et al., 2018) from the European Centre for Medium-Range Weather Forecasts
170   (ECMWF) at a resolution of $0.5°×0.5°$ and with 137 vertical levels. Since SF_6 is an almost nonreactive gas, removal processes are neglected in the calculation of the SRR.

In this study, five different backward calculation periods are investigated: 1, 5, 10, 20 and 50 days. At the end of these periods, particles are terminated and the back trajectories end. Figure 2 shows the 2012 annual average emission sensitivities for the backward calculation period of 5 (Fig. 2a) and 50 (Fig. 2b) days, respectively. On the 5 days time scale large land areas in the
175   Southern Hemisphere (Northern Australia, South America, Southern Africa) and also parts of the Northern Hemisphere (e.g. India, Iran) are sampled poorly or not at all. In these areas, emissions can therefore not be determined well by the inversion. High sensitivity can only be found at land regions with many receptors, such as Europe. On the 50 days time scale, the SRR has higher values compared to the 5 days backward calculation. Large parts of the Northern Hemisphere are sampled quite well and the emission sensitivities provide some information, even at areas that are far away from the observation stations.
180   However, emission sensitivities are still low in the Tropics, especially over Africa, South America and Northern Australia. When also using surface flask measurements (Fig. 2c) in addition to *in situ* measurements for the case of a 50 day backward simulation period, the emission sensitivity is substantially higher almost everywhere and more smoothly distributed over the globe. However, regions of low sensitivity remain in the Tropics and in the Southern Hemisphere.

2.4   The baseline definition

185   The transport model can only account for mixing ratio changes caused by emissions within the chosen backward calculation period. Consequently, a baseline representing the influence of all the emission contributions prior to this time period has to be defined.
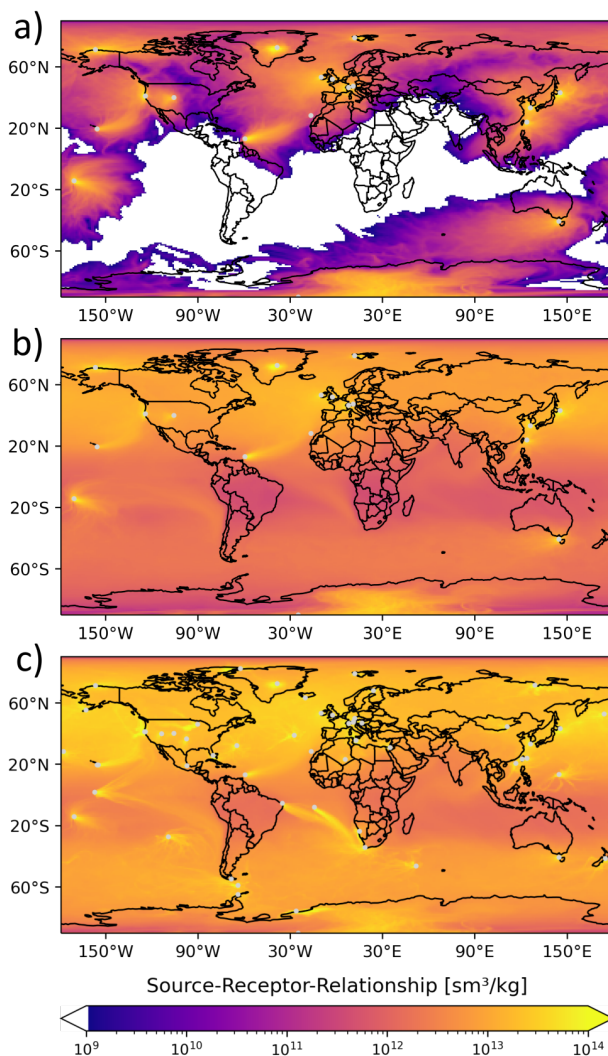
Figure 2. Source-Receptor-Relationship obtained from FLEXPART backward simulations, averaged over the year 2012. a) and b) show the SRR for all considered *in situ* measurement stations and for a simulation period of a) 5 and b) 50 days. c) shows the SRR for the case of using surface flask measurement sites in addition to *in situ* measurements and for a 50 day simulation period. Station locations are marked with grey dots.

2.4.1 The REBS method

The REBS method introduced by Ruckstuhl et al. (2012) is a statistical method using a robust local regression model to identify

190 background observations from each individual observation station to estimate a baseline curve. In recent years it has been used in various studies to determine a baseline for atmospheric inversions of several GHG species (e.g. An et al., 2012; Brunner et al., 2017; Henne et al., 2016; Schoenenberger et al., 2018; Simmonds et al., 2016; Vollmer et al., 2016). The REBS method

defines observed mixing ratios $y(t_i)$ at each time step t_i as the sum of a baseline signal $g(t_i)$, an enhancement due to polluted air masses $m(t_i)$ and the observational error E_i:

$$y(t_i) = g(t_i) + m(t_i) + E_i \tag{5}$$

195

The method assumes that most observations are baseline observations and therefore not influenced during pollution episodes ($m(t_i) = 0$). It also assumes that the baseline curve g is smooth - so that it can be linearly approximated around any given time. The method then applies a local linear regression model that fits the observation data, giving more weight to data points close to the considered time and iteratively excluding data points outside a certain range. An advantage of the REBS method is that it is simple to implement. The code is freely available and besides some parameters that need to be chosen, it only depends on the observation data. This simplicity, however, also means that the method is unable to take the length of the LPDM backward calculation into account. As we shall see, this leads to systematic biases in the inversion results that depend on the length of the backward calculation. The method also assumes a smoothly varying baseline which limits its ability to account for meteorological variability. Another disadvantage is the dependence on certain parameter settings. The settings used in this study are provided in Table A3. Finally, the method can only be used at sites with frequent observations, not for flask measurement sites, or moving measurement platforms.

2.4.2   Stohl's method

The method introduced by Stohl et al. (2009) is primarily based on the selection of observed mixing ratios at individual observation stations, but also uses the simulated SRR values and *a priori* emissions to determine the baseline. In the last few years it was used in several inversion studies (e.g. Brunner et al., 2017; Fang et al., 2014, 2015, 2019; Stohl et al., 2010; Thompson and Stohl, 2014). We apply the method and select the lowest 25 percent of observations from individual stations in a moving time window of 30 days to only consider observations which are weakly influenced by emissions within the backward calculation period. Prior simulated mixing ratio enhancements are subtracted from the selected observations to eliminate the emission contributions from within the time interval of the LPDM simulation. In order to avoid an overestimation of their contribution, only the lower half of the prior simulated values and the corresponding observed data points are selected. In every time window resulting mixing ratios are averaged and finally linearly interpolated to the timestamp of the observations. By subtracting prior simulated mixing ratios the method takes the length of the LPDM backward calculation into account and aims to avoid an overestimation of the baseline. However, simulated mixing ratios are calculated using *a priori* emission estimates, making the method dependent on *a priori* information. Further, the subjective choice of the time window, as well as the equally subjective selection of the lowest quartile of observations and the lower half of prior simulated mixing ratios are problematic. As the REBS method, Stohl's method assumes a smooth baseline curve, and thus it cannot account for sudden changes in the baseline due to meteorological variability. Also, the method can only be used at sites with frequent observations.
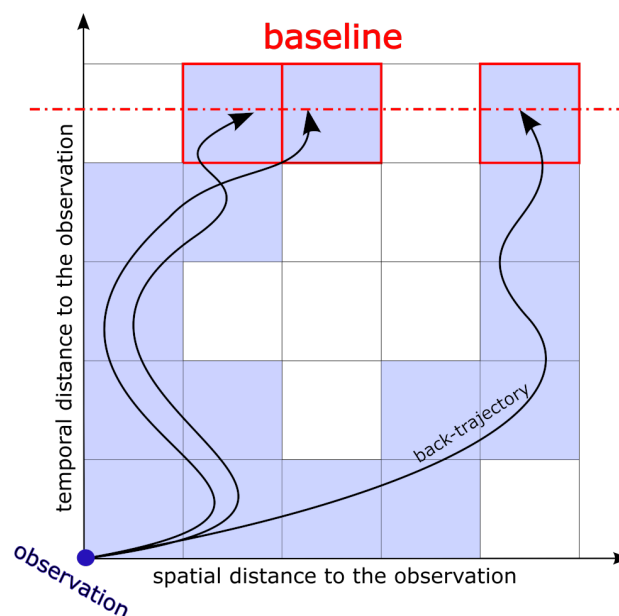
Figure 3. Simplified illustration of the global-distribution based (GDB) method for baseline determination, where the backward simulation is represented by three back trajectories released at the time and space of a particular observation. The spatio-temporal grid is simplified to two dimensions with a vertical time and a horizontal space axis. Grid cells that contribute to the modeled mixing ratio through emissions are shaded blue; termination grid cells where termination sensitivity is stored are marked with red rectangles; the termination point is illustrated by a red dashed horizontal line.

2.4.3 The GDB method

The idea of the GDB approach (Thompson and Stohl, 2014) is to determine the baseline directly from a 3D global field of

225   mixing ratios, e.g., from a re-analysis of the atmospheric chemical composition. The end points of the back-trajectories that are used by the LPDM to calculate the SRR are utilized to determine the sensitivity at the receptor to mixing ratios at the points in space and time where particles terminate (see Fig. 3 for a simplified illustration). This sensitivity (termed as "termination sensitivity", thereafter) in a particular grid cell is calculated in the LPDM by dividing the number of particles terminating in that cell by the total number released at the receptor, while also including a transmission function to account for loss processes

230   (not relevant for SF_6) during the backward simulation period. The termination sensitivity fields are saved in a 3D $1° \times 1°$ output grid with 16 vertical layers with interface heights at 0.1, 0.5, 1, 2, 3, 4, 5, 7, 9, 12, 15, 20, 25, 30, 40, and 50 km above ground level. For global inversions, baseline mixing ratios are then calculated by multiplying the termination sensitivity with the mixing ratios of the 3D global field and integrating the product over all grid cells. The GDB method can also be used for regional inversions (not done in this study). In this case, the emission contributions from outside the regional domain need to

235   be added to the baseline (Thompson and Stohl, 2014) but otherwise the inversion procedure is identical as described here.

The GDB method is independent of subjective data selection and choice of parameter settings. In contrast to the REBS and Stohl's method it does not assume a smooth baseline and has the potential to fully account for meteorological variability. As illustrated, it excludes emission contributions from within the backward simulation period and therefore provides a baseline that is fully consistent with the length of the backward simulation. Furthermore, contrary to the other two methods, it can also be

240 used at measurement sites with infrequent observations or moving observation platforms. Its accuracy, however, is dependent on the ability to eliminate errors, and especially any bias of the global 3D mixing ratio fields. We target this challenge by using the FLEXible PARTicle dispersion chemical transport model (FLEXPART CTM, Henne et al., 2018) to perform a re-analysis of SF_6 as described in the next section.

2.5 Re-analysis of SF_6 using FLEXPART CTM

245 In this study the LPDM FLEXPART 8-CTM-1.1 is used to perform a re-analysis of SF_6 for the year 2012. It was developed by Henne et al. (2018) and is based on FLEXPART 8.0. Groot Zwaaftink et al. (2018) provide a detailed description of FLEXPART CTM and evaluate it for the example of methane. FLEXPART CTM is run in a domain filling mode where 12 million particles are randomly distributed over the globe, proportional to the air density. In addition to an air tracer, particles also carry the chemical species SF_6. The initialisation is based on a latitudinal SF_6 profile based on surface observations. We

250 run the simulation from 2011 to 2012, using 2011 as a spin up period. Particles are followed forward in time, and whenever a particle resides below the diagnosed boundary layer height its mass is increased due to surface SF_6 emissions. The model is driven with the ECMWF ERA5 dataset and with emission fields calculated as described in section 2.6 . Mixing ratio fields are saved in a $3° \times 2°$ output grid and extrapolated to the same grid as the termination sensitivity fields.

FLEXPART CTM uses a nudging routine to keep simulated SF_6 fields close to the observations of SF_6. With this simple

255 data assimilation method, modeled fields of mixing ratios are relaxed towards observations within so-called nudging kernels around observation sites. For all surface observation stations in the Southern Hemisphere we assign relatively large uniform kernel sizes, since the model tends to overestimate SF_6 mixing ratios in the Southern Hemisphere and there are only few measurement stations to correct this bias. For the surface observation sites in the Northern Hemisphere, we assigned smaller kernel sizes to measurement stations with a large observation variability to conserve SF_6 spatial variability, especially over the

260 continents (see Groot Zwaaftink et al., 2018). For the aircraft measurements we pre-define vertical levels at 0.05, 0.15, 0.3, 0.5, 0.75, 0.1, 1.5, 2, 2.5, 3, 3.5, 4, 5, 6, 7, 8 and 9 km above ground level, co-locate the individual measurements to the closest vertical level and chose kernel sizes that increase with altitude. Specific kernel settings are detailed in Table A4.

2.6 *A priori* information

An *a priori* estimate of the spatial distribution of SF_6 emissions for the year 2012 is determined by collecting information on

265 the emissions from individual countries. We use country emissions reported to the United Nations Framework Convention on Climate Change (UNFCCC, 2021) and for East Asian countries emissions estimated by Fang et al. (2014). The sum of these individual country emissions is subtracted from the total global SF_6 emissions determined by Simmonds et al. (2020) and the remaining emissions are distributed to all other countries proportional to their electric power consumption (World Bank,

2021). Finally, total country emissions are disaggregated according to the gridded population density (CIESIN, 2018) within
270 each country's borders. The *a priori* emission uncertainty is estimated to be 50% in each grid cell with a minimal value of
$1 \cdot 10^{-13} \frac{kg}{m^2 h}$. Spatial and temporal correlation between uncertainties are considered by using an exponential decay model with
a scale length of 250 km and 30 days. The error covariance matrix **B** is calculated as the Kronecker product of the spatial and
temporal covariance matrices.

3 Results

3.1 Baselines and length of backward simulation

The three investigated baseline methods are discussed for the example of two measurement sites, Gosan and Ragged Point, and
for five backward simulation time periods. The Gosan observation station is located on the south-western tip of the Korean Is-
land Jeju, monitors the outflows from the Asian continent, and is respresentative of stations which frequently measure pollution
events. The Ragged Point observation station is situated on the eastern edge of Barbados with direct exposure to the Atlantic
280 Ocean. Ragged Point is primarily influenced by easterly winds providing "clean" background air masses, uninfluenced by local
emissions, and is therefore representative of background stations. Baseline mixing ratios are plotted together with respective
observations and *a priori* mixing ratios for different LPDM backward simulation periods ranging from 1 to 50 days. *A priori*
mixing ratios are calculated as the sum of the baseline and the contribution originating from *a priori* emissions during the
period of the backward simulation (termed "direct emissions contributions" thereafter). Ideally, the choice of the backward
285 simulation period should have no systematic effect on the calculated *a priori* mixing ratios. By increasing the backward sim-
ulation time, and therefore enlarging the temporal domain, more direct emission contributions are included. All these direct
emission contributions should be removed from the baseline and as a result the baseline should become lower and smoother
in order to leave *a priori* mixing ratios unchanged. Furthermore, one can assume that a correctly working baseline method
leads to a proper agreement between *a priori* mixing ratios and observations. This agreement is investigated here for the three
290 methods with time series plots (Fig. 4-7), as well as statistical parameters (bias, mean squared error (MSE), and coefficient of
determination (r^2)) summarized in Table 2.

Figure 4 shows the smooth baselines calculated with the REBS and Stohl's method at the measurement station Gosan. In
the case of 1-day backward simulations (Fig. 4a/d) both methods show a poor agreement between modeled and observed
mixing ratios, as neither the smooth baselines nor the small direct emission contributions can reproduce the observed mixing
295 ratios during pollution episodes. This agreement becomes much better with longer backward simulation periods, when direct
emission contributions get more impact (Fig. 4b/e). The REBS baseline stays completely unchanged for different backward
simulation periods. Therefore, *a priori* mixing ratios grow with increasing simulation periods (Fig. 4b/c), as more direct emis-
sions contribute to the calculated total mixing ratio. For Gosan, the bias is negative for the 1-day simulation period but becomes
increasingly positive for longer simulation periods (Table 2). This systematically increasing bias is inherent to all purely obser-
300 vation based baseline methods and cannot be corrected without adding model information. In contrast, Stohl's baseline level
decreases with longer backward simulation periods as higher direct emission contributions are subtracted from the pre-selected
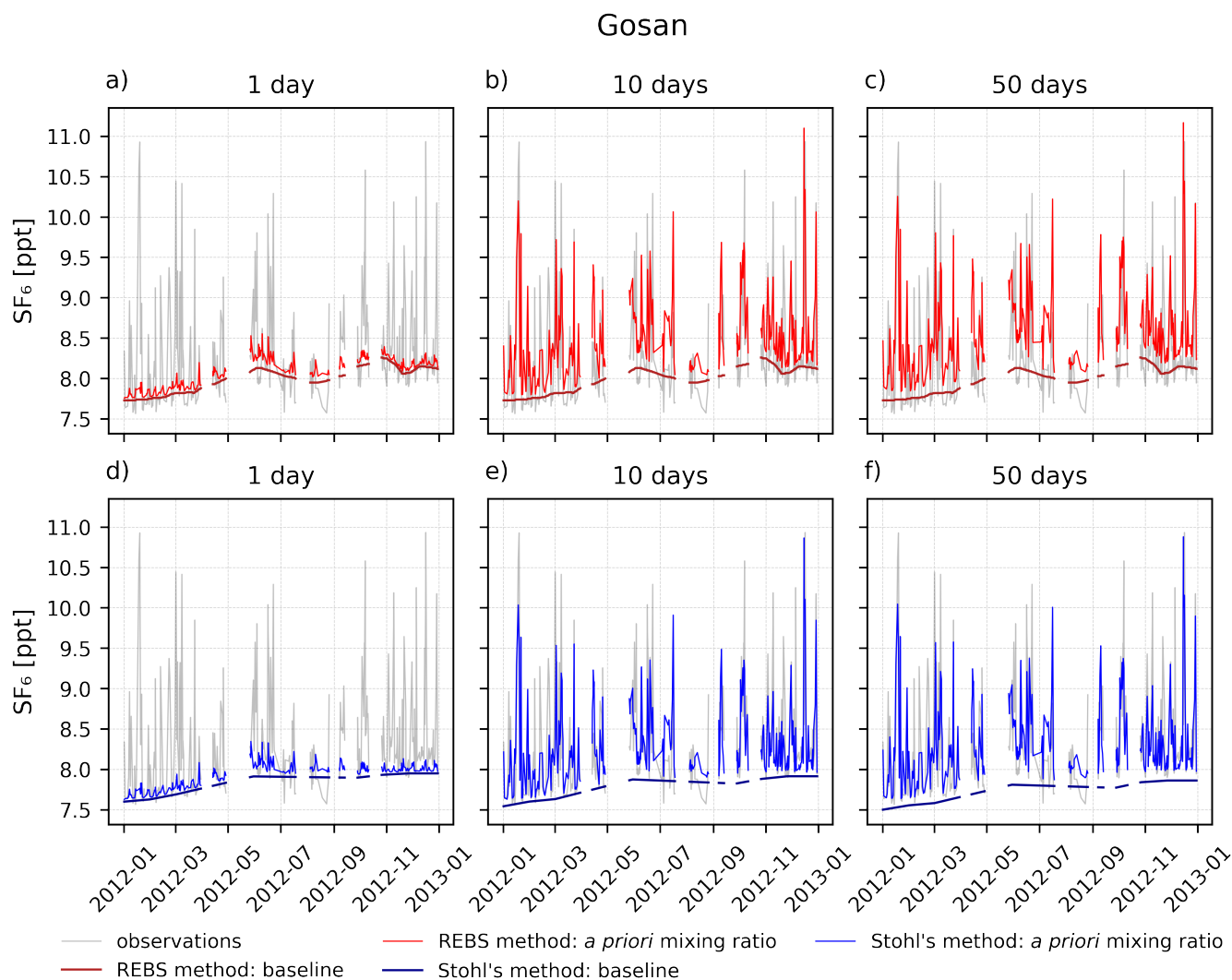
Figure 4. Baseline and *a priori* SF$_6$ mixing ratios calculated with the REBS (upper panels) and Stohl's method (lower panels) at the Gosan observation station, compared to SF$_6$ observations. Model results are shown for backward simulations of 1 day (panels a and d), 10 days (panels b and e) and 50 days (panels c and f).

Table 2. Bias, mean squared error (MSE) and coefficient of determination (r^2) of *a priori* SF$_6$ mixing ratios determined by the three investigated baseline methods with respect to observed mixing ratios. Statistical parameters are shown for three different backward calculation periods (1, 10, and 50 days) at the stations Gosan and Ragged Point. Also reported are the bias, MSE and r^2 calculated separately for all stations listed in Table 1, and then averaged.

Parameter	method	Gosan 1d	10d	50d	Ragged Point 1d	10d	50d	all stations 1d	10d	50d
	REBS	- 0.225	0.190	0.267	0.006	0.007	0.054	- 0.028	0.012	0.061
Bias [ppt]	Stohl	- 0.384	- 0.016	0.008	- 0.067	- 0.068	- 0.065	- 0.103	- 0.064	- 0.051
	GDB	- 0.090	-0.002	-0.006	0.023	0.044	0.033	0.022	0.016	0.007
	REBS	0.420	0.250	0.281	0.004	0.004	0.006	0.034	0.023	0.028
MSE [ppt^2]	Stohl	0.525	0.216	0.210	0.009	0.009	0.009	0.050	0.026	0.024
	GDB	0.303	0.206	0.205	0.005	0.005	0.004	0.034	0.022	0.021
	REBS	0.085	0.482	0.495	0.671	0.670	0.712	0.584	0.647	0.651
r^2	Stohl	0.068	0.474	0.490	0.649	0.629	0.623	0.548	0.616	0.623
	GDB	0.272	0.499	0.501	0.631	0.718	0.746	0.423	0.589	0.634

observations. Consequently, the bias of the *a priori* mixing ratios changes less between 10 and 50 days of backward simulation (Fig. 4e/f). This is confirmed by statistical parameters in Table 2, showing also only little change between 10 and 50 days.

At Ragged Point (Fig. 5) the *a priori* mixing ratios determined by the REBS method fit the observation data very well for
305 short backward simulation periods, where baseline and prior mixing ratios overlap because of small direct emission contributions (Fig. 5a/b). This is expected, since the method determines the baseline by fitting the observation data, while iteratively excluding outliers. Since Ragged Point is uninfluenced by regional emissions, no significant measurement peaks need to be excluded. Therefore, the REBS baseline fits well through the measurement data, resulting in a good statistical model-observation agreement (Table 2). However, the smooth baseline is unable to reproduce the observed variability. In the case of a simulation
310 period of 50 days (Fig. 5c), more direct emission contributions give higher *a priori* mixing ratios, overestimating the measurements and causing a large bias. In contrast, due to its 25th percentile pre-selection of observations, Stohl's method shifts the baseline curve towards the lower observations. For low direct emission contributions (Fig. 5a/b), *a priori* mixing ratios thus underestimate the observations. The resulting bias is almost unaffected by the different backward simulation periods (Table 2, Fig. 5c), showing the method's ability to compensate for increasing direct emission contributions. However, the rather ad hoc
315 25th percentile pre-selection of data for the baseline is obviously not justified for a background station with few pollution episodes, leading to a systematic underestimation of modeled *a priori* mixing ratios, irrespective of the length of the backward simulation.

The GDB method is illustrated for all tested backward simulation periods, including a case without any backward simulation (0 days). In this extreme case the baseline is obtained directly from the value of the global mixing ratio field simulated with
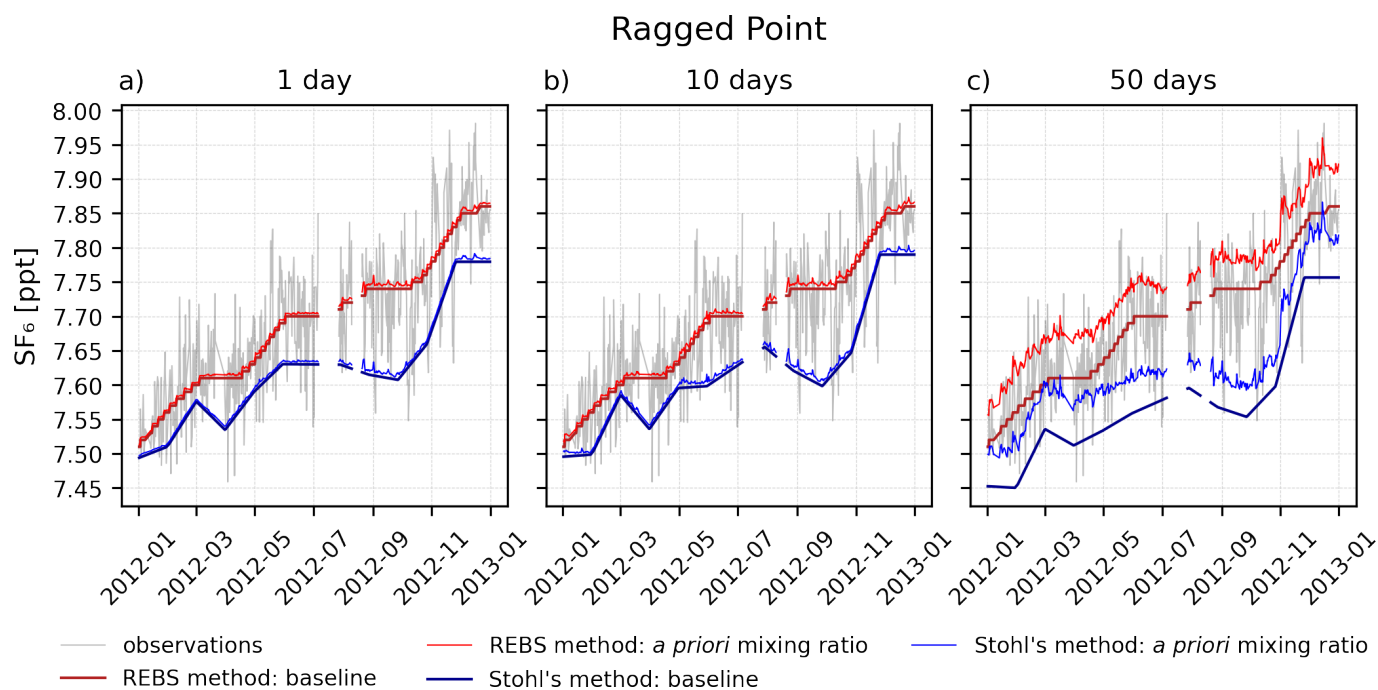
Figure 5. Baseline and *a priori* SF_6 mixing ratios determined by the REBS and Stohl's method at the Ragged Point observation station for backward simulation times of 1 day (panel a), 10 days (b) and 50 days (c).

320 FLEXPART CTM in the spatio-temporal grid cell of the respective observation. At Gosan, FLEXPART CTM reproduces observed mixing ratios well, even capturing a few pollution events (Fig. 6a). In the 1-day backward simulation case (Fig. 6b), the method computes a highly variable baseline partly representing the observed variability. This results in a much better agreement between *a priori* and observed mixing ratios than using the REBS or Stohl's method (Table 2). The GDB baseline becomes smoother and lower with increasing backward simulation time. The loss of variability arises from the fact that the

325 GDB method calculates the baseline from a weighted average of grid cell mixing ratios at the trajectory termination points. The longer particles are followed backward in time, the more widely dispersed over large geographical regions termination points become, thus resulting in a smoother baseline. The lowering of the GDB baseline is compensated by the increase of the direct emission contributions (see Section 2.4.3 and Fig. 3), ensuring a seamless transition between forward (Flexpart CTM) and backward simulations. As a result *a priori* mixing ratios in Fig. 6 show no large changes with increasing simulation period

330 between 5 and 50 days.

Figure 6 also demonstrates the advantage of the Lagrangian backward simulation. As FLEXPART CTM is limited in resolution and particle number, it can only reproduce a few pollution events at Gosan, underestimates the highest and overestimates the lowest measured SF_6 mixing ratios (Fig. 6a). The backward simulation is initiated at the exact location of the measurement point and provides, in principle, infinite resolution (Fig. 6b-f). If the backward calculation period is long enough that back tra-

335 jectories reach important emission regions, mixing ratio spikes similar to the observed ones can be simulated. At the same time,
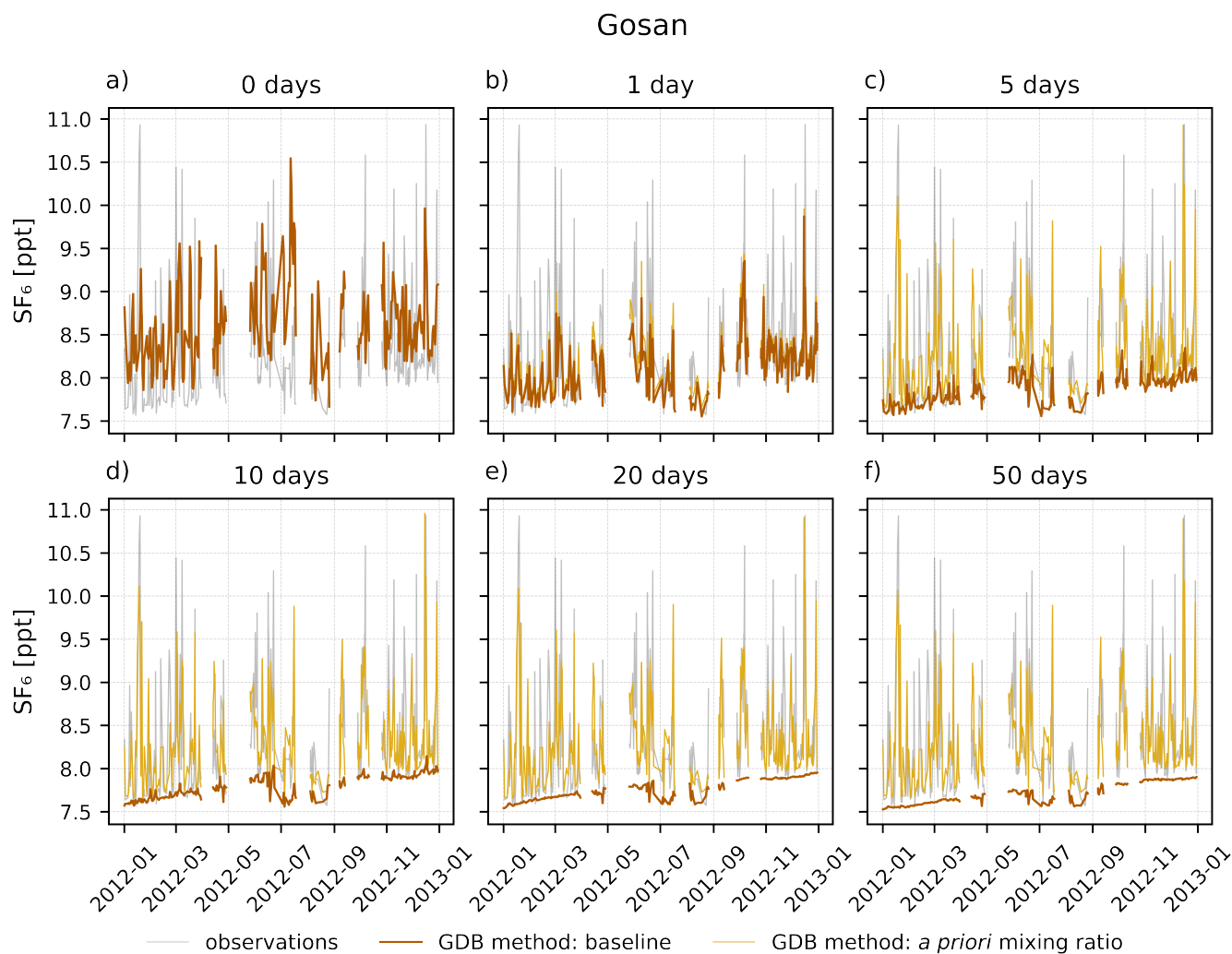
Figure 6. Baseline and *a priori* SF$_6$ mixing ratios calculated with the GDB method at the Gosan observation station for backward simulation times of 0 days (panel a), 1 day (b), 5 days (c), 10 days (d), 20 days (e) and 50 days (f).

Ragged Point
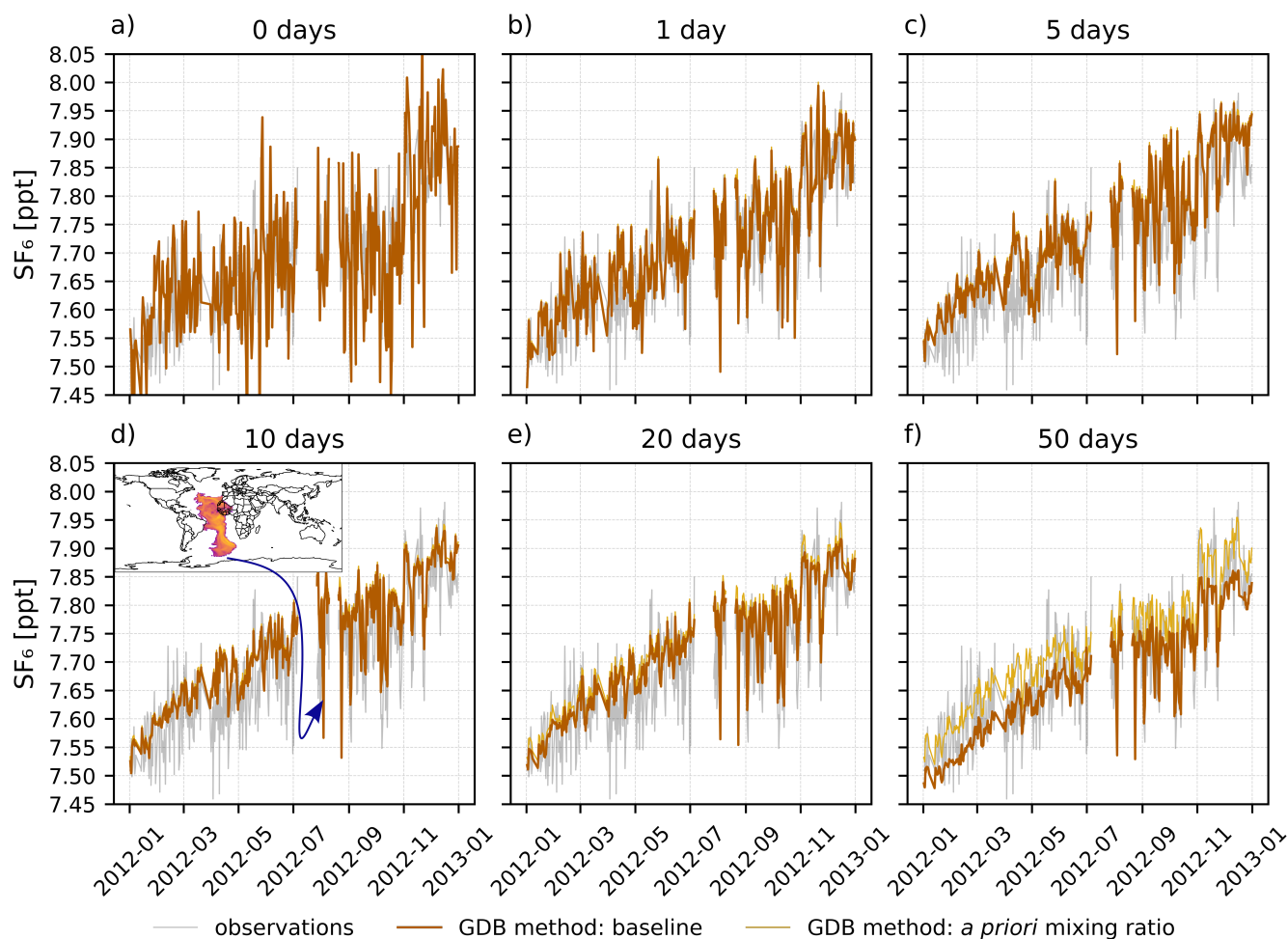
Figure 7. Baseline and *a priori* SF$_6$ mixing ratios calculated with the GDB method at the Ragged Point measurement station for backward simulation periods of 0 days (panel a), 1 day (b), 5 days (c), 10 days (d), 20 days (e) and 50 days (f). The inset in panel d shows the termination sensitivity averaged over all heights for the time of the marked observation low point, illustrating the methods ability to account for baseline changes, due to episodic transport from the Southern Hemisphere.

the lowered baseline for intrusions of southern air masses during the Asian summer monsoon also allows capturing the lowest observed values. As an indicator, Table 2 shows exclusively improving correlation between modeled and observed values with increasing backward simulation periods.

340   Figure 7 illustrates the GDB method at the Ragged Point station. FLEXPART CTM (Fig. 7a) reproduces the measured mixing ratios well, however generates more variability than observed at this station. This is partly due to the limited number of

particles in the domain-filling simulation, which introduces noise into the model results. This is averaged out by the GDB method with increasing backward simulation time, as the baseline becomes a weighted average over many grid cells. Nevertheless, the baseline maintains variability for all tested simulation periods, fitting the observed signal well (Fig. 7b-e). It is noteworthy that at Ragged Point a substantial part of the observed SF_6 variability seems to be caused by transport from dif-

345 ferent latitudes/regions without direct emission contributions, exemplified by the quite variable baseline even for the 50-day backward simulation. In contrast, the direct emissions accumulated over the 50 days of the backward simulation are producing an almost constant enhancement over the baseline. This is very different from a station like Gosan that is strongly influenced by pollution episodes.

Notice also that for backward simulation times of 10 days and longer, the combined FLEXPART CTM/backward model is

350 able to reproduce short episodes of very low observed mixing ratios at Ragged Point that are caused by episodic transport from the Southern Hemisphere (see also inset in Fig. 7d). Neither the REBS nor Stohl's method could correctly reproduce these negative SF_6 excursions.

Additional figures illustrating the three baseline methods at all investigated measurement sites, can be found in the supplementary material. Despite of all advantages of the GDB method, it reproduces measurements insufficiently if the modeled

355 global mixing ratio fields are biased. At Mace Head and Zeppelin (see supplementary Fig. S17 and S33), FLEXPART CTM overestimates the measurements, and thus the GDB method gives a baseline that partly exceeds the observations. At Mace Head, this could be explained to some extent by the close proximity of the station to the $3° \times 2°$ grid cell border resulting in the possibility that FLEXPART CTM attributes strong point emission contributions to the (relatively large) grid cells, that would be outside of the respective area of influence in reality. Other possible error sources include deficiencies in the emission

360 assumptions driving the model, that are impossible to be compensated through nudging with the few available observations. It is also unclear whether the FLEXPART CTM nudging routine was able to properly correct mixing ratios at higher altitudes, as aircraft measurements were available only over North America (with one exception).

Statistical parameters (bias, MSE, and r^2) were separately calculated for every observation station and respective averages over all stations are shown in Table 2. One should keep in mind that the REBS and Stohl's method are based on the observa-

365 tions themselves and thus the observed and modeled *a priori* mixing ratios are not independent. Therefore, it is remarkable that overall the GDB method obtains smaller bias and MSE values than the other two methods. Regarding correlation, it is not surprising, that Table 2 shows the largest r^2 values for the REBS method, where the baseline is basically a fit of the observation data. However, it is noteworthy that for the GDB method, the r^2 value improves systematically with growing backward simulation time and for 50 days even exceeds the value derived by Stohl's method. By extending the backward calculation

370 period from 10 to 50 days the GDB r^2 value increases by 0.045, meaning that an extra 4.5% of the observed variability can be explained by the model. This is quite a substantial improvement. Notice also the improvement in bias and MSE, which can be observed for the GDB and Stohl's method, when extending the simulation period from 10 to 50 days. The REBS method does not show these improvements due to its systematical increase of bias with backward simulation time.
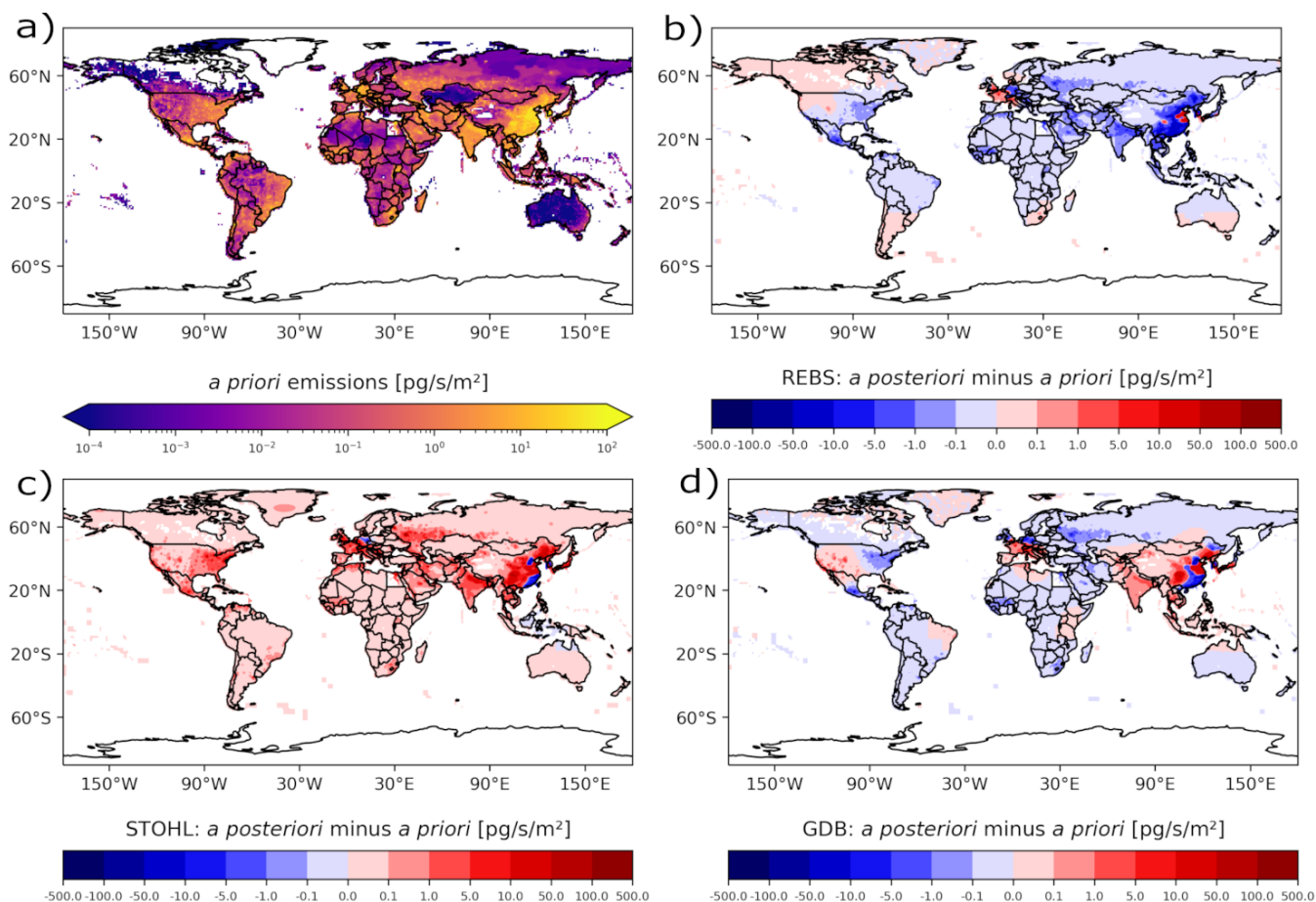
Figure 8. *A priori* SF$_6$ emissions (a) and SF$_6$ emission increments given by the inversion when using the REBS method (b), Stohl's method (c), and the GDB method (d) based on 20 day LPDM backward simulations.

3.2 Inversion Results

375   Figure 8 illustrates (a) the global distribution of the SF$_6$ *a priori* emissions 2012, as well as (b-d) the emission increments (i.e., *a posteriori* minus *a priori* emissions) for the three investigated baseline methods using SRRs from 20 days backward calculations. *A priori* emissions are allocated to regions proportional to electricity use and population density. This implies large *a priori* emissions in South and East Asia, including China which is estimated to be the biggest contributor to global SF$_6$ emissions. In general, much higher *a priori* emissions are allocated to the Northern than to the Southern Hemisphere. We

380   should also note that the emission optimization of the inversion focuses on regions with large *a priori* emissions, where also assumed uncertainties are bigger (see Section 2.6), assigning a larger degree of freedom to the algorithm.

The inversion increments in Fig. 8b-d show three very contrasting pictures, illustrating the huge impact of the choice of the baseline method on the inversion results. Using different baseline approaches completely changes the results of the inversions.
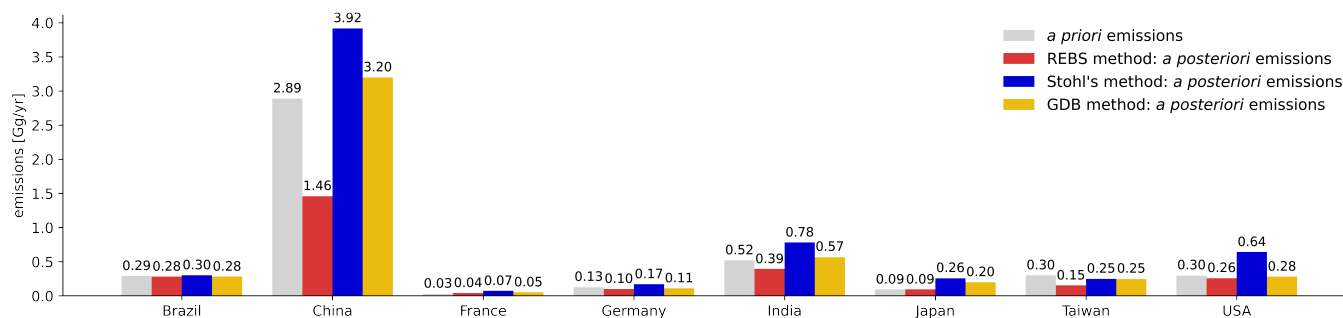
Figure 9. National SF$_6$ emissions for selected countries, based on 20 day LPDM backward calculations with different choices of the baseline method.

When using the REBS method (Fig. 8b), the inversion produces negative emission increments in almost all areas of the globe, indicating that calculated baselines are too high overall. This is consistent with the assumption that the method overestimates the baseline at individual stations by wrongly classifying observations as baseline observations that are actually influenced by emissions within the backward calculation period. In contrast, the inversion algorithm produces positive increments almost everywhere around the globe when applying Stohl's method (Fig. 8c), suggesting that the method systematically underestimates the baseline (not only at background stations) which generally leads to *a priori* emissions that are too high. In case of the GDB method (Fig. 8d) negative and positive increments are more balanced, showing no sign of a systematical under- or overestimation of the baseline. Large positive increments can be seen in East Asian regions and parts of Europe, whereas the inversion tends to produce slightly negative increments in the Southern Hemisphere.

National emissions

As the verification of emission reports to UNFCCC takes place on a national scale, the impact of baseline methods on national emissions is of great interest (Fig. 9). In countries with very low emission sensitivity (e.g., Brazil) inversion increments are very small in all three cases and the baseline choice has therefore little impact. However, considering countries with higher emission sensitivities (e.g., China), the *a posteriori* emissions are very sensitive to the baseline definition. In almost all cases the REBS method leads to smaller and Stohl's method to larger national emissions than the GDB method, again revealing systematic problems in the first two methods. Due to the large emissions in China these problems become especially apparent there, with almost a factor 3 emission difference, corresponding to almost 30% of the 2012 global SF$_6$ emissions.

Global emissions

The 2012 SF$_6$ global emissions are shown in Fig. 10. The bars represent inversion results using different backward calculation periods between 1 and 50 days (light to dark shading). The horizontal dashed line illustrates a reference value calculated by Simmonds et al. (2020) with the AGAGE 12-box model. Notice that this is the same value used to calculate the *a priori* emissions, so the line represents also the global *a priori* emissions. Since the uncertainty of the global emissions is relatively
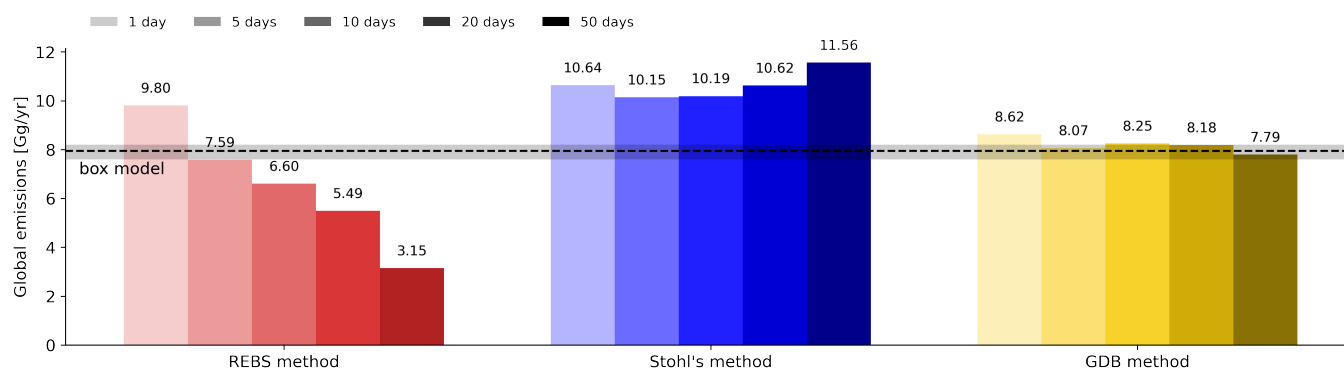
Figure 10. SF$_6$ global emissions derived by the inversions. Results are shown for the three applied baseline methods and for the five applied backward simulation periods between 1 and 50 days. The horizontal dashed line represents the reference value of the AGAGE 12-box model with shaded error bands.

small, global emissions derived by the inversion should roughly match the value of the box model, regardless which backward simulation period was used.

For the REBS method, calculated global emissions (red) decrease dramatically with growing backward simulation time, showing values between 3.15 Gg/yr and 9.80 Gg/yr. This is a consequence of the method's incapability to remove emission
410 contributions from the baseline when the backward simulation period expands, leading to a systematical overestimation of the baseline and underestimation of the emissions. The resulting bias increases with growing simulation period and as a result global emissions estimates deviate strongly from the box model.

In the case of Stohl's method (blue), derived global emissions do not show such a systematic decrease with longer backward simulation periods as observed for the REBS method. This is because Stohl's method not only selects low mixing ratio obser-
415 vations, but also uses model information to maintain the baseline. For longer backward simulation periods, higher simulated mixing ratios are subtracted from the pre-selected observations to compensate for more direct emission contributions. Nevertheless, global emissions significantly exceed the reference value of the box model for all applied simulation periods, implying a systematic overestimation of emissions through too low baselines. The overestimation of the global emissions increases with longer backward simulation times larger than 5 days. This suggests that the method overcompensates for additional direct
420 emission contributions when the simulation period expands, subtracting systematically too high values from the pre-selected observations.

Considering the inversion results based on the GDB method, global emissions are in good agreement with the box model result for all tested backward simulation periods. Furthermore, global emissions stay almost unchanged for different backward simulation periods, demonstrating again the method's ability to ensure a flawless transition between the forward (Flexpart
425 CTM) and backward calculation.
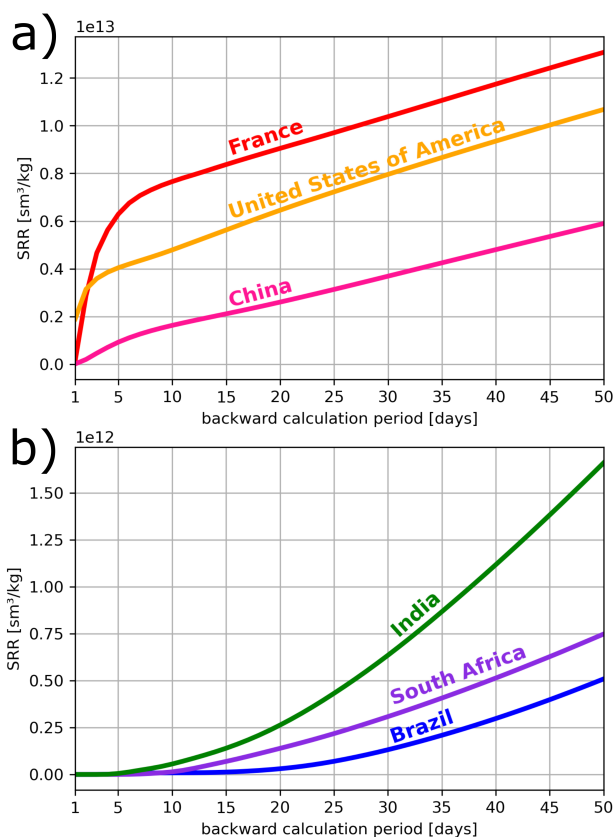
Figure 11. SRR for individual countries and different backward calculation periods between 1 to 50 days, considering all *in situ* measurement stations in Tab 1. The shown values are averages over the grid cells of a) France, USA, China and b) India, South Africa, Brazil, for the year 2012.

The advantage of longer backward simulation periods

As an argument for a relatively short backward simulation period Stohl et al. (2009) stated that "the value for the inversion of every additional simulation day decreases rapidly with time backward". Certainly, this is true for countries and regions that are well covered by the global monitoring network. For instance, for France the SRR increases rapidly in the first few backward

430   simulation days but flattens to a linear increase for longer backward simulation periods (Fig. 11a). A similar behavior can be observed for many countries in the Northern Hemisphere, although the curve's slope for the first few days varies. For countries poorly covered by the monitoring network, however, the SRR is close to zero for the first 5 to 15 backward days and increases exponentially afterwards (see Fig. 11b). For these poorly-monitored countries only backward simulations beyond the usual 5-10 days used in most studies provide information for the inversion. For these countries, the SRR increase with time flattens

435   to a linear increase only for very long transport times, even beyond the 50 days used in this study.
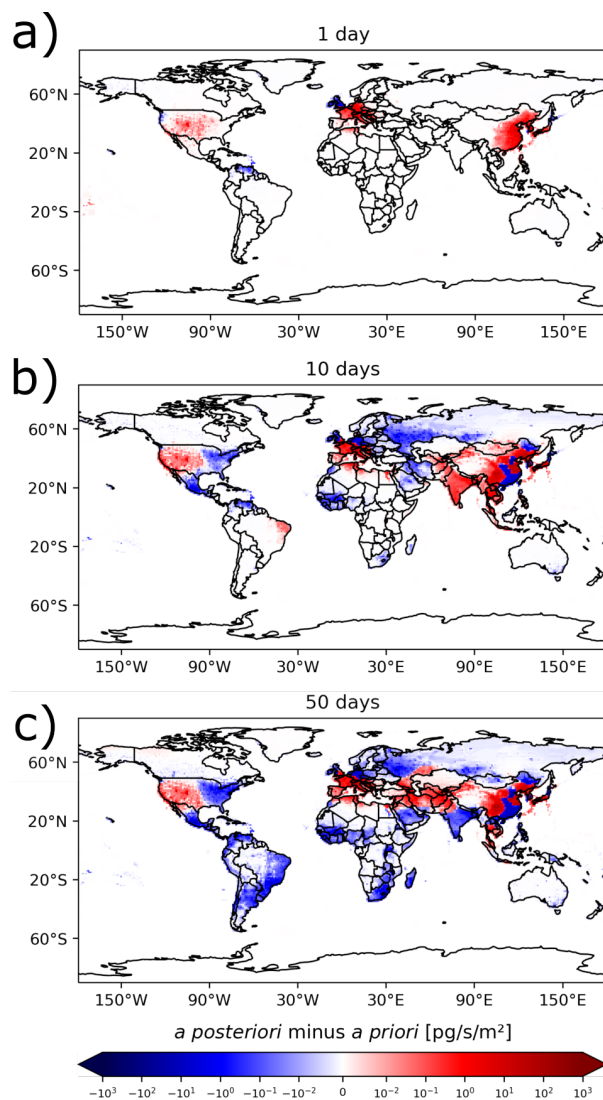
Figure 12. SF$_6$ emission increments calculated with the inversion by using the GDB method and a backward simulation period of a) 1 day, b) 10 days and c) 50 days
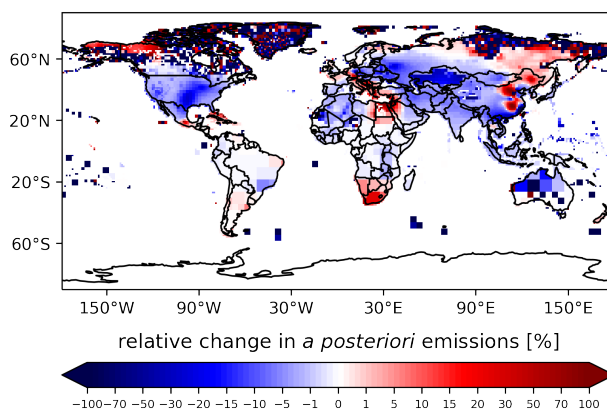
Figure 13. Relative change in *a posteriori* emissions, when using flask measurements in addition to *in situ measurements*.

Figure 12 further illustrates the impact of different backward simulation periods on the inversion, by showing emission increments for the GDB method and for backward simulation periods of 1, 10 and 50 days. In case of 1-day backward calculations (Fig. 12a) the inversion significantly optimizes *a priori* emissions only in East Asia and parts of Europe. As the backward simulation period is extended to 10 days (Fig. 12b), the inversion optimizes emissions in larger parts of the Northern Hemisphere but in the Southern Hemisphere emission increments are still small. In case of 50 days (Fig. 12c), the inversion optimizes emissions even far away from observation stations (e.g. South America or South Africa). In India, where SRR values are also small and *a priori* emissions (and thus emission uncertainties) are high (see also 11b), the emission increments even switch from positive to negative by extending the period from 10 to 50 days. Also, the calculated relative uncertainty reduction increases by extending the backward simulation period (see Fig. A2a-c).

The use of flask samples

An advantage of the GDB method is the possibility to include flask measurements from fixed sites or moving platforms in the inversion. By contrast, the REBS and Stohl's method require short measurement intervals at fixed sites for the statistical baseline calculation. Figure 13 shows the relative change in *a posteriori* emissions using flask measurements additionally to the *in situ* measurements for the 50 days backward simulation. One can see substantial differences in the USA, Eastern Europe, Asia, and Southern Africa, illustrating the great value of this additional information. Further, the inclusion of flask measurements slightly increases the relative error reduction in their surroundings (e.g. USA, South Africa, see Fig. A2c,d).

Reliable global emissions can only be obtained with long backward simulation periods

In previous sections, we have used global mixing ratio fields from the GDB method where great care has been taken to avoid biases that would affect the baseline, and we have used global *a priori* emissions that correspond to the rather well known global SF_6 emissions. These are optimal conditions for the inversion that are rarely fulfilled for other species than SF_6. For
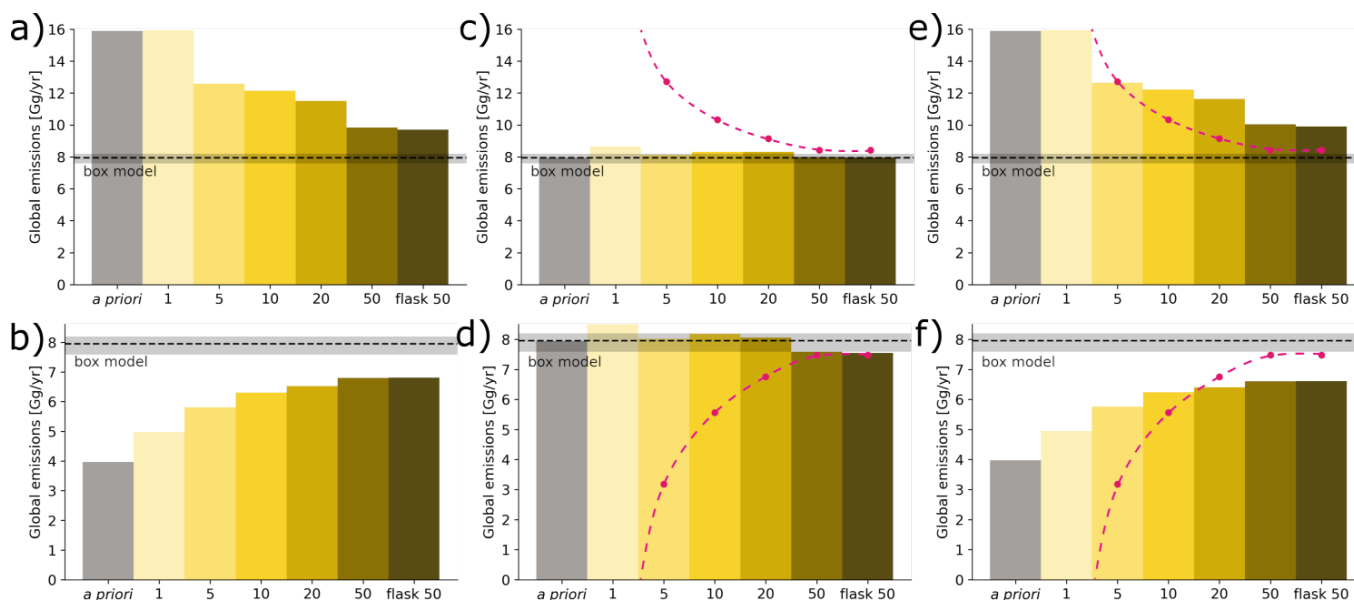
Figure 14. Global SF$_6$ emissions using the GDB method shown for different sensitivity cases, using backward simulation periods between 1 and 50 days, and a 50 days backward simulation case, where additionally to *in situ* measurements also flask measurements were included in the inversion. The sensitivity cases include a) doubled and b) halved *a priori* emissions; biased global mixing ratio fields with a uniform bias of c) -0.003 ppt and d) +0.003 ppt in every grid cell; and combinations of the two test types; e) doubled *a priori* emissions plus -0.003 ppt global field bias; f) halved *a priori* emissions plus +0.003 ppt global field bias. The dashed red lines indicate the emissions that would result from attributing the global field bias in the global mixing ratio fields to emissions during the backward simulation period.

many species global emissions are less well known, and with fewer observations than for SF$_6$ also the global distribution (and, thus, the baseline) is more uncertain. However, a skillful inversion should tolerate such biases and still produce reliable results. While we lack information for verifying that regional emissions are reliable, for SF$_6$ we can at least test whether global emissions can be determined by our inversion in the presence of biases.

460   Figure 14 shows global *a posteriori* emissions when biases in (1) the *a priori* emissions and (2) global mixing ratio fields were added. This is shown for different backward simulation periods between 1 and 50 days and for the 50 days case with inclusion of flask measurements. Note here that for all these sensitivity cases we use the same absolute *a priori* emission uncertainties, as for the original *a priori* emissions without any artificial bias.

Comparing the inversion results for doubled (Fig. 14a) and halved (Fig. 14b) *a priori* emissions clearly shows that the
465   corresponding biases in the global *a posteriori* emissions are reduced substantially with increasing backward simulation period and converge towards the rather well known global SF$_6$ emission from the box model. However, it is clear that a substantial bias remains even with a backward simulation period of 50 days. It seems likely that an extension of the backward simulation period beyond 50 days would further reduce the bias. The inclusion of flask measurements leads to slight additional improvements.

Another sensitivity test was performed with artificially biased global mixing ratio fields by subtracting (Fig. 14c) or adding
470 (Fig. 14d) 0.003 ppt from/to the FLEXPART CTM model output in every grid cell of the 3D mixing ratio fields. 0.003 ppt
is equivalent to roughly 1% of the 2012 global mixing ratio increase and thus corresponds to about 3 days of global SF_6
emissions. To still fit the model to the observations, the inversion will try to compensate such a bias in the baseline with a
bias of the opposite sign in the emissions. As always, the inversion can only attribute this additional bias to emissions within
the simulation period. Therefore, shorter backward simulation periods require a greater modification of emissions than longer
475 periods, in order to compensate for the baseline bias. To fully compensate the baseline bias equivalent to 3 days of emissions,
global *a posteriori* emissions (dashed, pink line) would need to deviate strongly from the box model value for the 1 days case,
but converge towards it with increasing backward simulation time. In fact, with a positive baseline bias negative emissions
would be required for backward simulation times of less than 3 days, as the baseline exceeds the observations. The inversion
results do not show this extreme behavior, since for short backward simulation times high SRR values are found only in small
480 regions, and the emission changes there are bound by the prescribed *a priori* uncertainties. Notice that in our case of a known
added bias, this is rather a shortcoming, as this shows that the inversion is not able to compensate the baseline bias for short
backward simulation times. Only for the longest times, the emissions converge towards the expected global emissions (dashed
pink lines), and only for such long backward simulation times baseline biases equivalent to 3 days of emissions become
negligible.

485 Finally, we also combined doubled *a priori* emissions with a -0.003 ppt bias in the global mixing ratio fields (Fig. 14e) and
halved *a priori* emissions with a +0.003 ppt bias (Fig. 14f). For both cases, the inversion becomes less sensitive to biases in the
a priori emissions and the global fields with longer backward simulation periods.

4   Conclusions

We have examined the use of LPDMs for inverse modeling of GHG emissions by varying the backward simulation period in
490 the range of 1 to 50 days, testing several methods for estimating a baseline, investigating the influence of biases in the *a priori*
emissions and the baseline, and exploring the value of flask measurements for the inversion. We found the following:

- A baseline method that is purely based on the observations at the observation site itself, such as the REBS method, leads
  to unreliable inversion results that are highly sensitive to the length of the LPDM backward simulation and can lead to
  entirely unrealistic *a posteriori* global total emissions. For instance, for the year 2012 inversions with the REBS method
495 produce *a posteriori* global total SF_6 emissions of 9.8 Gg/yr and 3.2 Gg/yr for backward simulation periods of 1 day and
  50 days, respectively, compared to a well known reference value of around 8.0 Gg/yr.

- A baseline method that is based on the observations at the site itself but corrects for emissions occurring during the
  LPDM backward simulation period leads to smaller sensitivity to the backward calculation time but may still lead to
  substantially biased emissions irrespective of backward simulation period. For instance, inversions with Stohl's method
500 overestimate the well known 2012 SF_6 global total emissions by 2.2 - 3.6 Gg/yr (28-45%).

   – A global distribution based (GDB) approach, where the LPDM backward simulation is nested into a global mixing ratio field, is superior and leads to *a posteriori* emissions that are far less sensitive to the LPDM backward calculation length and that are consistent with global total emissions. In contrast to station-specific baselines, the GDB method allows the inclusion of low-frequency measurements (e.g., flask samples) or data from mobile platforms into the inversion.

505   – Statistical comparisons of *a priori* modeled versus observed mixing ratios show that longer LPDM backward simulations outperform shorter simulations. In particular, extending the trajectory length from the usual 5-10 days to 50 days reduces the mean squared error and increases the correlation. .

   – Inverse modelling is highly sensitive to biases in the *a priori* emissions as well as biases in the baseline. We could show that this sensitivity decreases with the length of the backward simulation period. While it is nearly impossible to

510   correct biased global *a priori* emissions with backward simulation periods of 1-10 days, 50-day backward simulations can capture global emissions quite accurately even in the presence of large biases.

   – The additional use of flask measurements improves the observational constraint on SF_6 emissions substantially. However, existing flask sampling sites are often not well located for inversion purposes. We suggest that placing a few additional flask sampling sites downwind of potential emission regions in currently undersampled regions (in particular, tropical

515   South America, tropical Africa, India, Australia and the Maritime Continent) would have disproportionately large value for improving regional and global *a posteriori* emission fields.

Following these results, we strongly recommend to abandon the use of baseline methods based purely on the observations of individual sites, for inverse modeling. We also recommend to employ longer LPDM backward simulation periods, beyond the usual 5-10 days, as this leads to improvements in overall model performance, allows to constrain emissions in regions poorly

520 covered by the monitoring network, and produces more robust global emission estimates. When consistency between regional and global emission estimates is important, even longer backward simulation periods than 50 days may be useful. Finally, we suggest to take additional flask measurements at continental sites in the Tropics and Southern Hemisphere as they would greatly enhance inversion-derived global emission fields.

Code and data availability. The used source codes of FLEXPART 10.4 and FLEXINVERT+ (with small modifications to the original version

525 freely available at https://flexinvert.nilu.no/download.html; downloaded in July 2020; (described in detail by Thompson and Stohl, 2014)) are provided at https://doi.org/10.25365/phaidra.339, together with input-, setting- and output data. The source code of FLEXPART 8-CTM-1.1 together with an users guide can be freely downloaded at https://doi.org/10.5281/zenodo.1249190. The source code of FLEXPART 10.4 is also freely available on the FLEXPART website: https://www.flexpart.eu/downloads (described in detail by Pisso et al., 2019). Atmospheric measurements of SF_6 mixing ratios used in this study are freely available from the following sources: AGAGE data: http://agage.eas.gatech.

530 edu/data_archive/, NOAA ESRL data: https://gml.noaa.gov/dv/data/, NOAA Carbon Cycle Group ObsPack data: https://doi.org/10.25925/20180817, World Data Centre for Greenhouse Gase: https://gaw.kishou.go.jp/. All the listed websites were last accessed on 27.04.2022.

Author contributions. MV and AS designed the study with contributions from RT. MV performed the FLEXPART, FLEXPART CTM, and FLEXINVERT+ simulations. RT helped with the FLEXINVERT+ setup and simulation issues. MV made the figures with help from AP. MV wrote the text with input from AS, AP, and RT.

535 *Competing interests.* The authors declare that they have no conflict of interest.

Acknowledgements. We thank the whole AGAGE team for providing measurement data, including J. Mühle (Scripps Institution of Oceanography); P.B. Krummel, P.J. Fraser, L.P. Steele (CSIRO Oceans and Atmosphere); R. Wang (Georgia Institute of Technology); S. O'Doherty, D. Young (University of Bristol); M.K. Vollmer, S. Reimann (EMPA: Swiss Federal Laboratories for Materials Science and Technology); C.R. Lunder, O. Hermanson (NILU: Norwegian Institute for Air Research). AGAGE operations at Mace Head, Trinidad Head, Cape
540 Matatula, Ragged Point, and Cape Grim are supported by NASA (USA) grants to MIT (NAG5-12669, NNX07AE89G, NNX11AF17G, NNX16AC98G) and SIO (NNX07AE87G, NNX07AF09G, NNX11AF15G, NNX11AF16G, NNX16AC96G, NNX16AC97G), and also by: Department for Business, Energy & Industrial Strategy (BEIS, UK), Contract 1537/06/2018 to the University of Bristol for Mace Head and NOAA (USA), contract 1305M319CNRMJ0028 to the University of Bristol for Ragged Point; CSIRO and BoM (Australia): FOEN grants to Empa (Switzerland); NILU (Norway); SNU (Korea); CMA (China); NIES (Japan); and Urbino University (Italy). For Jungfraujoch funding
545 is acknowledged for the project HALCLIM/CLIMGAS-CH by the Swiss Federal Office for the Environment (FOEN) and for ICOS (Integrated Carbon Observation System) by the Swiss National Science Foundation. In addition, measurements are supported by the International Foundation High Altitude Research Stations Jungfraujoch and Gornergrat (HFSJG). The Commonwealth Scientific and Industrial Research Organisation (CSIRO, Australia) and Bureau of Meteorology (Australia) are thanked for their ongoing long-term support and funding of the Cape Grim station and the Cape Grim science program. We also thank the NOAA Global Monitoring Laboratory for providing access to their
550 data, including G. Dutton, J.W. Elkins, B. Hall, C. Sweeney, E. Dlugokencky, A. Andrews, D. Nance, and keypartners: L. Huang (EC), K. Davis (PSU), S. Biraud (LBNL-ARM). We further acknowledge following people and institutions for sharing their observation data: T. Saito (National Institute for Environmental Studies, Japan); S. Park, M. Park (Kyungpook National University - operations of the Gosan station on Jeju Island, South Korea were supported by the National Research Foundation of Korea grant funded by the Korean government MSIT no. 2020R1A2C3003774); E. Cuevas (State Meteorological Agency, Spain); D.Say (University of Bristol). We also thank C. Groot Zwaaftink, S.
555 Eckhardt (NILU), and S. Henne (EMPA) for providing and supporting with the Flexpart CTM model. Further acknowledgement is made for the use of ECMWF's computing and archive facilities provided through a special project (spatvojt) in this research. We further thank Marina Dütsch, Lucie Bakels, Sivia Bucci, Katharina Baier, Daria Tatsii, and Perta Seibert for their support.

Table A1. Surface flask measurement sites

Site ID	Station	Latitude	Longitude	Altitude[a]
ALT	Alert, Canada	82.5°N	62.5°W	190
ASC	Ascension Island, UK	8.0°S	14.4°W	90
ASK	Assekrem, Algeria	23.3°N	5.6°E	2715
AZR	Serreta (Terceira), Portugal	38.8°N	27.4°W	24
BAL	Baltic Sea, Poland	55.4°N	17.2°E	28
BHD	Baring Head, New Zealand	41.4°S	174.9°E	90
BKT	Bukit Kototabang, Indonesia	0.2°S	100.3°E	875
BMW	Tudor Hill (Bermuda), UK	32.3°N	64.9°W	60
BSC	Constanta (Black Sea), Romania	44.2°N	28.7°E	5
CBA	Cold Bay (AK), USA	55.2°N	162.7°W	57
CHR	Christmas Island, Kiribati	1.7°N	157.2°W	5
CPT	Cape Point, South Africa	34.4°S	18.5°E	260
CRZ	Crozet, France	46.4°S	51.8°E	202
DRP	Drake Passage, USA	59.0°S	63.7°W	10
DSI	Dongsha Island, Taiwan	20.7°N	116.7°E	8
EIC	Easter Island, Chile	27.2°S	109.4°W	69
GMI	Guam (Mariana Island), USA	13.4°N	144.7°E	5
HBA	Halley, UK	75.6°S	26.2°W	35
HFM	Harvard Forest (MA), USA	42.5°N	72.2°W	1000
HPB	Hohenpeissenberg, Germany	47.8°N	11.0°E	941
HSU	Humboldt State University, USA	41.0°N	124.7°W	8
HUN	Hegyhatsal, Hungary	47.0°N	16.6°E	344
ICE	Storhofdi, Iceland	63.4°N	20.3°W	127
KEY	Key Biscane (FL), USA	25.7°N	80.2°W	6
KUM	Cape Kumukahi (HI), USA	19.5°N	154.8°W	8
LEF	Park Falls (WI), USA	45.9°N	90.3°W	868
LLN	Lulin, Taiwan, Province of China	23.5°N	120.9°E	2867
LMP	Lampedusa, Italy	35.5°N	12.6°E	50
MEX	Mex High Altitude Global Climate Observation Center, Mexico	19.0°N	97.3°W	4469
MID	Sand Island, USA	28.2°N	177.4°W	16
MKN	Mt. Kenya, Kenya	0.1°S	37.3°E	3649
NAT	Natal, Brazil	5.5°S	35.3°W	20
NMB	Gobabeb, Namibia	23.6°S	15.0°E	461
OXK	Ochsenkopf, Germany	50.0°N	11.8°E	1172
PAL	Pallas, Finland	68.0°N	24.1°E	570
PSA	Palmer Station, USA	64.9°S	64.0°W	15
PTA	Point Arena (CA), USA	39.0°N	123.7°W	22
SGP	Southern Great Plains E13 (OK), USA	36.6°N	97.5°W	374
SHM	Shemya Island, USA	52.7°N	174.1°E	28
TIK	Tiksi, Russian Federation	71.6°N	128.9°E	29
USH	Ushuaia, Argentina	54.8°S	68.3°W	32
UTA	Wendover (UT), USA	39.9°N	113.7°W	1332
UUM	Ulaan Uul, Mongolia	44.5°N	111.1°E	1012
WIS	Sede Boker, Israel	30.9°N	34.8°E	482

[a] The altitude specifies the sampling height in meters above sea level.

Table A2. Aircraft flask measurement programs

Site ID	Aircraft Programs	Latitude	Longitude	Altitude^a
BNE	Beaver Crossing, Nebraska, United States	40.8°N	97.2°W	616 - 7855
CAR	Briggsdale, Colorado, United States	40.7°N	104.3°W	1795 - 8469
CMA	Cape May, New Jersey, United States	38.9°N	74.3°W	280 - 8010
DND	Dahlen, North Dakota, United States	47.5°N	99.1°W	587 - 8023
ESP	Estevan Point, British Columbia, Canada	49.4°N	126.4°W	246 - 5740
ETL	East Trout Lake, Saskatchewan, Canada	54.3°N	104.9°W	811 - 7823
HIL	Homer, Illinois, United States	40.0°N	87.9°W	555 - 8051
LEF	Park Falls, Wisconsin, United States	46.0°N	90.2°W	583 - 4018
NHA	Worcester, Massachusetts, United States	42.9°N	70.5°W	245 - 8069
PFA	Poker Flat, Alaska, United States	64.8°N	148.2°W	222 - 7444
RTA	Rarotonga, Cook Islands	21.2°S	159.8°W	15 - 6483
SCA	Charleston, South Carolina, United States	32.9°N	79.5°W	218 - 8070
SGP	Southern Great Plains, Oklahoma, United States	36.6°N	97.5°W	437 - 5716
TGC	Sinton, Texas, United States	27.7°N	96.7°W	250 - 8074
THD	Trinidad Head, California, United States	41.1°N	124.2°W	231 - 8034
WBI	West Branch, Iowa, United States	41.7°N	91.3°W	591 - 8204

^{a} The altitude specifies the range of sampling heights in meters above sea level.

Table A3. Setting parameters of the REBS method. For more information see Ruckstuhl et al. (2012).

Setting Parameters	Description
b = 2.5	tuning factor which governs the weight of outliers in the baseline
$span = \frac{1}{6}$	the ratio of observation points used to compute one baseline value. (the goal is a temporal window of 2 months). It regulates the amount of baseline smoothing.
maxit = c(10, 10)	maximum number of iterations

Table A4. Nudging kernel settings for surface and aircraft measurement sites. The kernels are set to have an equal spatial length (in meters) in the x and the y direction. For surface measurement sites in the northern hemisphere, an upper limit for h_y was set to 25°; σ_{obs} defines the standard deviation of measurements over the simulation period at each nudging location; σ_{max} describes the maximum value of σ_{obs} from all surface observation stations. For aircraft measurement sites, the kernel size depends on the height level above ground H. For additional information on the parameters see Groot Zwaaftink et al. (2018)

surface measurements sites				
hemisphere	spatial kernel width h_y [°]	kernel height h_z [m]	temporal kernel length h_t [s]	kernel relaxation time τ [s]
northern hemisphere	$h_y = \frac{\sigma_{max}}{\sigma_{obs}} \cdot 2$	$h_z = 300$	$h_t = 86,400 \cdot \frac{\sigma_{max}}{\sigma_{obs}}$	$\tau = 3600$
southern hemisphere	$h_y = 25$	$hz = 500$	$h_t = 86,400 \cdot \frac{\sigma_{max}}{\sigma_{obs}}$	$\tau = 3600$
aircraft measurements sites				
height H [km above ground]	spatial kernel width h_y [°]	kernel height h_z [m]	temporal kernel length h_t [s]	kernel relaxation time τ [s]
$H \leqslant 0.5$	$h_y = 10$	$h_z = 100$	$h_t = 86,400 \cdot \frac{h_y}{1°}$	$\tau = 3600$
$0.5 < H \leqslant 1$	$h_y = 20$	$h_z = 250$	$h_t = 86,400 \cdot \frac{h_y}{1°}$	$\tau = 3600$
$1 < H \leqslant 2$	$h_y = 30$	$h_z = 500$	$h_t = 86,400 \cdot \frac{h_y}{1°}$	$\tau = 3600$
$2 < H \leqslant 3$	$h_y = 40$	$h_z = 500$	$h_t = 86,400 \cdot \frac{h_y}{1°}$	$\tau = 3600$
$3 < H \leqslant 4$	$h_y = 50$	$h_z = 500$	$h_t = 86,400 \cdot \frac{h_y}{1°}$	$\tau = 3600$
$4 < H \leqslant 5$	$h_y = 60$	$h_z = 500$	$h_t = 86,400 \cdot \frac{h_y}{1°}$	$\tau = 3600$
$5 < H \leqslant 6$	$h_y = 70$	$h_z = 1000$	$h_t = 86,400 \cdot \frac{h_y}{1°}$	$\tau = 3600$
$6 < H \leqslant 7$	$h_y = 80$	$h_z = 1000$	$h_t = 86,400 \cdot \frac{h_y}{1°}$	$\tau = 3600$
$7 < H \leqslant 8$	$h_y = 90$	$h_z = 1000$	$h_t = 86,400 \cdot \frac{h_y}{1°}$	$\tau = 3600$
$8 < H \leqslant 9$	$h_y = 100$	$h_z = 1000$	$h_t = 86,400 \cdot \frac{h_y}{1°}$	$\tau = 3600$
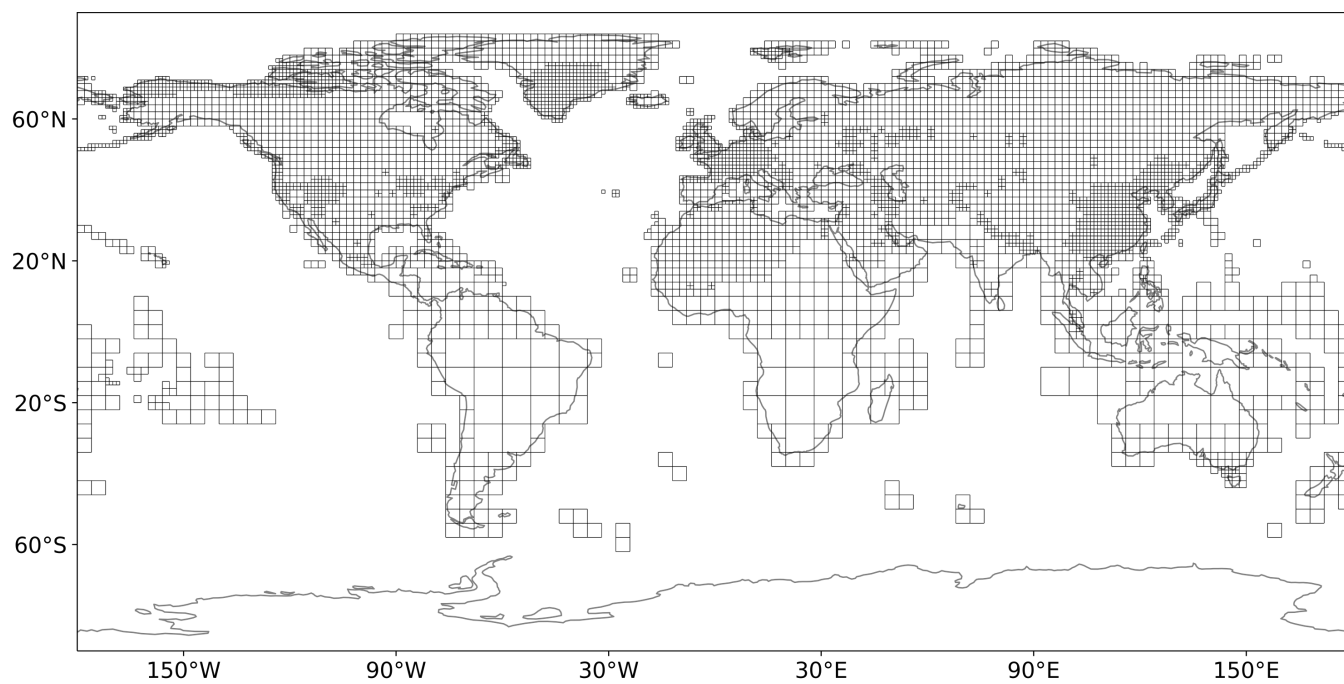
Figure A1. Variable-resolution grid on which emissions are optimized by the inversion.
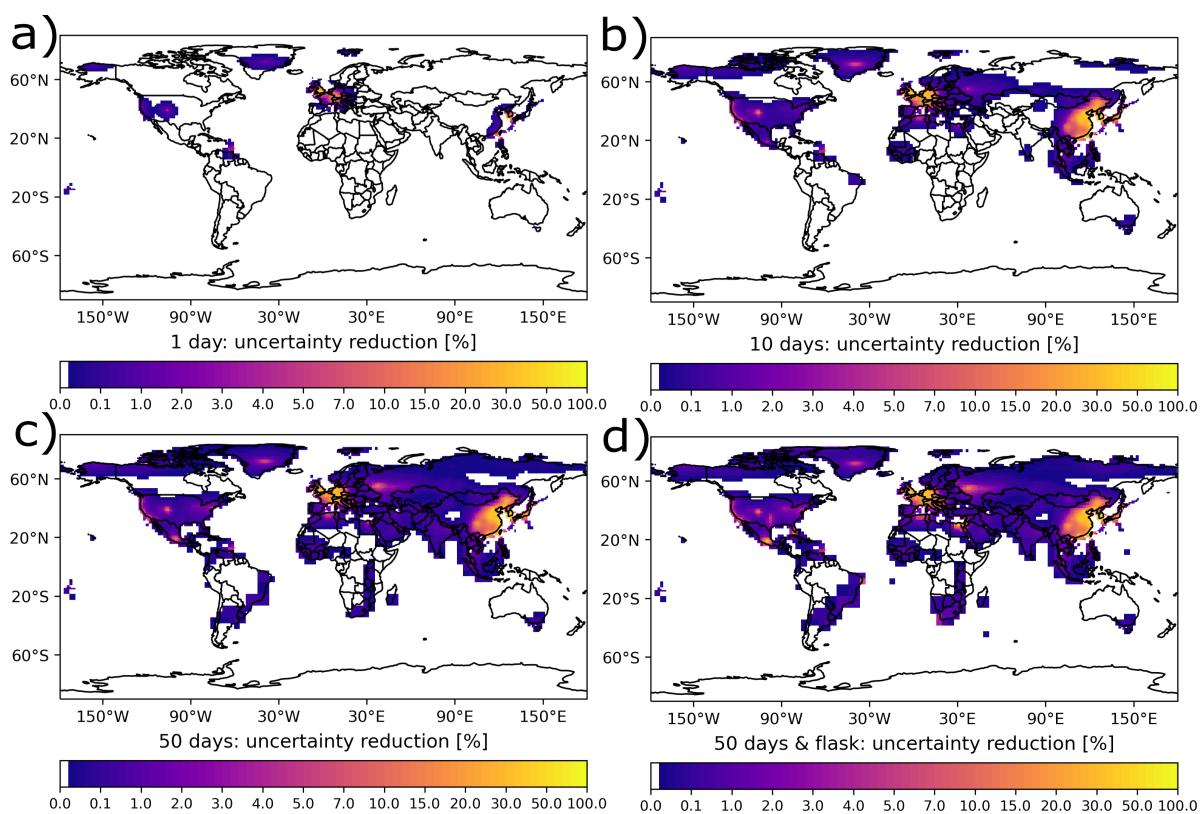
Figure A2. Relative uncertainty reductions ($1 - \frac{u_{post}}{u_{pri}}$) calculated with the inversion by using the GDB method and a backward simulation period for a) 1 day, b) 10 days, c) 50 days, and d) for the 50 days case, where also flask measurements were included

References

An, X., Henne, S., Yao, B., Vollmer, M. K., Zhou, L., and Li, Y.: Estimating emissions of HCFC-22 and CFC-11 in China by atmospheric observations and inverse modeling, Science China Chemistry, 55, 2233–2241, https://doi.org/10.1007/s11426-012-4624-8, 2012.

Berchet, A., Sollum, E., Thompson, R. L., Pison, I., Thanwerdas, J., Broquet, G., Chevallier, F., Aalto, T., Berchet, A., Bergamaschi, P., Brunner, D., Engelen, R., Fortems-Cheiney, A., Gerbig, C., Groot Zwaaftink, C. D., Haussaire, J.-M., Henne, S., Houweling, S., Karstens, U., Kutsch, W. L., Luijkx, I. T., Monteil, G., Palmer, P. I., van Peet, J. C. A., Peters, W., Peylin, P., Potier, E., Rödenbeck, C., Saunois, M., Scholze, M., Tsuruta, A., and Zhao, Y.: The Community Inversion Framework v1.0: a unified system for atmospheric inversion studies, Geoscientific Model Development, 14, 5331–5354, https://doi.org/10.5194/gmd-14-5331-2021, 2021.

Brunner, D., Arnold, T., Henne, S., Manning, A., Thompson, R. L., Maione, M., O'Doherty, S., and Reimann, S.: Comparison of four inverse modelling systems applied to the estimation of HFC-125, HFC-134a, and SF$_6$ emissions over Europe, Atmospheric Chemistry and Physics, 17, 10 651–10 674, https://doi.org/10.5194/acp-17-10651-2017, 2017.

CIESIN: Center for International Earth Science Information Network, Columbia University, Gridded Population of the World, Version 4 (GPWv4): Population Density, Revision 11. Palisades, NY: NASA Socioeconomic Data and Applications Center (SEDAC), https://doi.org/10.7927/H49C6VHW, last accessed: 2022-04-27, 2018.

Dlugokencky, E., Crotwell, A., Mund, J., Crotwell, M., and Thoning, K.: Atmospheric Sulfur Hexafluoride Dry Air Mole Fractions from the NOAA GML Carbon Cycle Cooperative Global Air Sampling Network, 1997-2019, Version: 2020-07, https://doi.org/10.15138/p646-pa37, 2020.

Dutton, G., Elkins, J., Hall, B., and NOAA ESRL: Earth System Research Laboratory Halocarbons and Other Atmospheric Trace Gases Chromatograph for Atmospheric Trace Species (CATS) Measurements, Version 1. NOAA National Centers for Environmental Information., https://doi.org/10.7289/V5X0659V, last accessed: 2022-04-27, 2017.

Fang, X., Thompson, R. L., Saito, T., Yokouchi, Y., Kim, J., Li, S., Kim, K. R., Park, S., Graziosi, F., and Stohl, A.: Sulfur hexafluoride (SF6) emissions in East Asia determined by inverse modeling, Atmospheric Chemistry and Physics, 14, 4779–4791, https://doi.org/10.5194/acp-14-4779-2014, 2014.

Fang, X., Stohl, A., Yokouchi, Y., Kim, J., Li, S., Saito, T., Park, S., and Hu, J.: Multiannual Top-Down Estimate of HFC-23 Emissions in East Asia, Environmental Science & Technology, 49, 4345–4353, https://doi.org/10.1021/es505669j, 2015.

Fang, X., Yao, B., Vollmer, M. K., Reimann, S., Liu, L., Chen, L., Prinn, R. G., and Hu, J.: Changes in HCFC Emissions in China During 2011–2017, Geophysical Research Letters, 46, 10 034–10 042, https://doi.org/10.1029/2019GL083169, 2019.

Ganesan, A. L., Rigby, M., Zammit-Mangion, A., Manning, A. J., Prinn, R. G., Fraser, P. J., Harth, C. M., Kim, K.-R., Krummel, P. B., Li, S., Mühle, J., O'Doherty, S. J., Park, S., Salameh, P. K., Steele, L. P., and Weiss, R. F.: Characterization of uncertainties in atmospheric trace gas inversions using hierarchical Bayesian methods, Atmospheric Chemistry and Physics, 14, 3855–3864, https://doi.org/10.5194/acp-14-3855-2014, 2014.

Groot Zwaaftink, C. D., Henne, S., Thompson, R. L., Dlugokencky, E. J., Machida, T., Paris, J.-D., Sasakawa, M., Segers, A., Sweeney, C., and Stohl, A.: Three-dimensional methane distribution simulated with FLEXPART 8-CTM-1.1 constrained with observation data, Geoscientific Model Development, 11, 4469–4487, https://doi.org/10.5194/gmd-11-4469-2018, 2018.

Guillevic, M., Vollmer, M. K., Wyss, S. A., Leuenberger, D., Ackermann, A., Pascale, C., Niederhauser, B., and Reimann, S.: Dynamic–gravimetric preparation of metrologically traceable primary calibration standards for halogenated greenhouse gases, Atmospheric Measurement Techniques, 11, 3351–3372, https://doi.org/10.5194/amt-11-3351-2018, 2018.

595   Henne, S., Brunner, D., Oney, B., Leuenberger, M., Eugster, W., Bamberger, I., Meinhardt, F., Steinbacher, M., and Emmenegger, L.: Valida-
           tion of the Swiss methane emission inventory by atmospheric observations and inverse modelling, Atmospheric Chemistry and Physics,
           16, 3683–3710, https://doi.org/10.5194/acp-16-3683-2016, 2016.

       Henne, S., Brunner, D., Groot Zwaaftink, C. D., and Stohl, A.: FLEXPART 8-CTM-1.1: Atmospheric Lagrangian Particle Dispersion Model
           for global tracer transport, https://doi.org/10.5281/zenodo.1249190, last accessed: 2022-04-27, 2018.

600   Hersbach, H., de Rosnay, P., Bell, B., Schepers, D., Simmons, A., Soci, C., Abdalla, S., Alonso-Balmaseda, M., Balsamo, G., Bechtold, P.,
           Berrisford, P., Bidlot, J.-R., de Boisséson, E., Bonavita, M., Browne, P., Buizza, R., Dahlgren, P., Dee, D., Dragani, R., Diamantakis, M.,
           Flemming, J., Forbes, R., Geer, A., Haiden, T., Hólm, E., Haimberger, L., Hogan, R., Horányi, A., Janiskova, M., Laloyaux, P., Lopez, P.,
           Munoz-Sabater, J., Peubey, C., Radu, R., Richardson, D., Thépaut, J.-N., Vitart, F., Yang, X., Zsótér, E., and Zuo, H.: Operational global
           reanalysis: progress, future directions and synergies with NWP, https://doi.org/10.21957/tkic6g3wm, series: ERA Report, 2018.

605   IPCC: Summary for Policymakers, in: Global Warming of 1.5°C. An IPCC Special Report on the impacts of global warming of 1.5°C
           above pre-industrial levels and related global greenhouse gas emissions pathways, in the context of strengthening the global response to
           the threat of climate change, sustainable development, and efforts to eradicate poverty, edited by Masson-Delmotte, V., Zhai, P., Pörtner,
           H. O., Roberts, D., Skea, J., Shukla, P. R., Pirani, A., Moufouma-Okia, W., Péan, C., Pidcock, R., Connors, S., Matthews, J. B. R., Chen,
           Y., Zhou, X., Gomis, M. I., Lonnoy, E., Maycock, T., Tignor, M., and Waterfield, T., p. 32, World Meteorological Organization, Geneva,
610   Switzerland, https://ipcc.ch/report/sr15, 2018.

       Keller, C. A., Hill, M., Vollmer, M. K., Henne, S., Brunner, D., Reimann, S., O'Doherty, S., Arduini, J., Maione, M., Ferenczi, Z., et al.:
           European emissions of halogenated greenhouse gases inferred from atmospheric measurements, Environmental science & technology, 46,
           217–225, https://doi.org/10.1021/es202453j, 2012.

       Maione, M., Graziosi, F., Arduini, J., Furlani, F., Giostra, U., Blake, D. R., Bonasoni, P., Fang, X., Montzka, S. A., O'Doherty, S. J., Reimann,
615   S., Stohl, A., and Vollmer, M. K.: Estimates of European emissions of methyl chloroform using a Bayesian inversion method, Atmospheric
           Chemistry and Physics, 14, 9755–9770, https://doi.org/10.5194/acp-14-9755-2014, 2014.

       Miller, B. R., Weiss, R. F., Salameh, P. K., Tanhua, T., Greally, B. R., Mühle, J., and Simmonds, P. G.: Medusa: A Sample Preconcentra-
           tion and GC/MS Detector System for in Situ Measurements of Atmospheric Trace Halocarbons, Hydrocarbons, and Sulfur Compounds,
           Analytical Chemistry, 80, 1536–1545, https://doi.org/10.1021/ac702084k, 2008.

620   Monteil, G. and Scholze, M.: Regional CO_2 inversions with LUMIA, the Lund University Modular Inversion Algorithm, v1.0, Geoscientific
           Model Development, 14, 3383–3406, https://doi.org/10.5194/gmd-14-3383-2021, 2021.

       Myhre, G., Shindell, D., Bréon, F.-M., Collins, W., Fuglestvedt, J., Huang, J., Koch, D., Lamarque, J.-F., Lee, D., Mendoza, B., Nakajima, T.,
           Robock, A., Stephens, G., Takemura, T., and Zhang, H.: Anthropogenic and natural radiative forcing, pp. 659–740, Cambridge University
           Press, Cambridge, UK, https://doi.org/10.1017/CBO9781107415324.018, 2013.

625   NOAA Carbon Cycle Group ObsPack Team: Multi-laboratory compilation of atmospheric sulfure hexafluoride data for the
           period 1983-2017; obspacksf61v2.1.12018−08−17; NOAA Earth System Research Laboratory, Global Monitoring Division,
           https://doi.org/10.15138/g3ks7p, 2018.

       NOAA ESRL: NOAA Earth System Research Laboratoriy: Sulfur Hexafluoride (SF6) WMO Scale, https://gml.noaa.gov/ccl/sf6_scale.html,
           last accessed: 2022-05-27, 2014.

630   Pisso, I., Sollum, E., Grythe, H., Kristiansen, N. I., Cassiani, M., Eckhardt, S., Arnold, D., Morton, D., Thompson, R. L., Groot Zwaaftink,
           C. D., Evangeliou, N., Sodemann, H., Haimberger, L., Henne, S., Brunner, D., Burkhart, J. F., Fouilloux, A., Brioude, J., Philipp, A.,

Seibert, P., and Stohl, A.: The Lagrangian particle dispersion model FLEXPART version 10.4, Geoscientific Model Development, 12, 4955–4997, https://doi.org/10.5194/gmd-12-4955-2019, 2019.

Prinn, R., Weiss, R., Fraser, P., Simmonds, P., Cunnold, D., Alyea, F., O'doherty, S., Salameh, P., Miller, B., Huang, J., et al.: A history of
635   chemically and radiatively important gases in air deduced from ALE/GAGE/AGAGE, Journal of Geophysical Research: Atmospheres,
        105, 17 751–17 792, https://doi.org/10.1029/2000JD900141, 2000.

Prinn, R. G., Weiss, R. F., Arduini, J., Arnold, T., DeWitt, H. L., Fraser, P. J., Ganesan, A. L., Gasore, J., Harth, C. M., Hermansen, O., Kim,
        J., Krummel, P. B., Li, S., Loh, Z. M., Lunder, C. R., Maione, M., Manning, A. J., Miller, B. R., Mitrevski, B., Mühle, J., O'Doherty, S.,
        Park, S., Reimann, S., Rigby, M., Saito, T., Salameh, P. K., Schmidt, R., Simmonds, P. G., Steele, L. P., Vollmer, M. K., Wang, R. H., Yao,
640   B., Yokouchi, Y., Young, D., and Zhou, L.: History of chemically and radiatively important atmospheric gases from the Advanced Global
        Atmospheric Gases Experiment (AGAGE), Earth System Science Data, 10, 985–1018, https://doi.org/10.5194/essd-10-985-2018, 2018.

Ravishankara, A. R., Solomon, S., Turnipseed, A. A., and Warren, R. F.: Atmospheric lifetimes of long-lived halogenated species, Science
        (New York, N.Y.), 259, 194–199, https://doi.org/10.1126/science.259.5092.194, 1993.

Rigby, M., Manning, A. J., and Prinn, R. G.: Inversion of long-lived trace gas emissions using combined Eulerian and Lagrangian chemical
645   transport models, Atmospheric Chemistry and Physics, 11, 9887–9898, https://doi.org/10.5194/acp-11-9887-2011, 2011.

Rigby, M., Park, S., Saito, T., Western, L. M., Redington, A. L., Fang, X., and Henne, S.: Increase in CFC-11 emissions from eastern China
        based on atmospheric observations, Nature, 569, 546–550, https://doi.org/10.1038/s41586-019-1193-4, 2019.

Ruckstuhl, A. F., Henne, S., Reimann, S., Steinbacher, M., Vollmer, M. K., O'Doherty, S., Buchmann, B., and Hueglin, C.: Robust ex-
        traction of baseline signal of atmospheric trace species using local regression, Atmospheric Measurement Techniques, 5, 2613–2624,
650   https://doi.org/10.5194/amt-5-2613-2012, 2012.

Ryall, D. B., Derwent, R. G., Manning, A. J., Simmonds, P. G., and O'Doherty, S.: Estimating source regions of European emissions of
        trace gases from observations at Mace Head, Atmospheric Environment, 35, 2507–2523, https://doi.org/10.1016/S1352-2310(00)00433-
        7, 2001.

Rypdal, K., Stordal, F., Fuglestvedt, J., and Berntsen, T.: Introducing top-down methods in assessing compliance with the Kyoto Protocol,
655   Climate Policy, 5, 393–405, https://doi.org/10.1080/14693062.2005.9685565, 2005.

Rödenbeck, C., Gerbig, C., Trusilova, K., and Heimann, M.: A two-step scheme for high-resolution regional atmospheric trace gas inversions
        based on independent models, Atmospheric Chemistry and Physics, 9, 5331–5342, https://doi.org/10.5194/acp-9-5331-2009, 2009.

Saito, T.: private communication, feb. 05, 2021.

Saito, T., Yokouchi, Y., Stohl, A., Taguchi, S., and Mukai, H.: Large Emissions of Perfluorocarbons in East Asia Deduced from Continuous
660   Atmospheric Measurements, Environmental Science & Technology, 44, 4089–4095, https://doi.org/10.1021/es1001488, 2010.

Schoenenberger, F., Henne, S., Hill, M., Vollmer, M. K., Kouvarakis, G., Mihalopoulos, N., O'Doherty, S., Maione, M., Emmenegger, L.,
        Peter, T., and Reimann, S.: Abundance and sources of atmospheric halocarbons in the Eastern Mediterranean, Atmospheric Chemistry and
        Physics, 18, 4069–4092, https://doi.org/10.5194/acp-18-4069-2018, 2018.

Seibert, P. and Frank, A.: Source-receptor matrix calculation with a Lagrangian particle dispersion model in backward mode, Atmospheric
665   Chemistry and Physics, 4, 51–63, https://doi.org/10.5194/acp-4-51-2004, 2004.

Simmonds, P. G., Rigby, M., Manning, A. J., Lunt, M. F., O'Doherty, S., McCulloch, A., Fraser, P. J., Henne, S., Vollmer, M. K., Mühle, J.,
        Weiss, R. F., Salameh, P. K., Young, D., Reimann, S., Wenger, A., Arnold, T., Harth, C. M., Krummel, P. B., Steele, L. P., Dunse, B. L.,
        Miller, B. R., Lunder, C. R., Hermansen, O., Schmidbauer, N., Saito, T., Yokouchi, Y., Park, S., Li, S., Yao, B., Zhou, L. X., Arduini,
        J., Maione, M., Wang, R. H. J., Ivy, D., and Prinn, R. G.: Global and regional emissions estimates of 1,1-difluoroethane (HFC-152a,

670   CH3CH2) from in situ and air archive observations, Atmospheric Chemistry and Physics, 16, 365–382, https://doi.org/10.5194/acp-16-365-2016, 2016.

Simmonds, P. G., Rigby, M., McCulloch, A., Vollmer, M. K., Henne, S., Mühle, J., O'Doherty, S., Manning, A. J., Krummel, P. B., Fraser, P. J., et al.: Recent increases in the atmospheric growth rate and emissions of HFC-23 (CHF 3) and the link to HCFC-22 (CHClF 2) production, Atmospheric Chemistry and Physics, 18, 4153–4169, https://doi.org/10.5194/acp-18-4153-2018, 2018.

675   Simmonds, P. G., Rigby, M., Manning, A. J., Park, S., Stanley, K. M., McCulloch, A., Henne, S., Graziosi, F., Maione, M., Arduini, J., Reimann, S., Vollmer, M. K., Mühle, J., O'Doherty, S., Young, D., Krummel, P. B., Fraser, P. J., Weiss, R. F., Salameh, P. K., Harth, C. M., Park, M.-K., Park, H., Arnold, T., Rennick, C., Steele, L. P., Mitrevski, B., Wang, R. H. J., and Prinn, R. G.: The increasing atmospheric burden of the greenhouse gas sulfur hexafluoride (SF6), Atmospheric Chemistry and Physics, 20, 7271–7290, https://doi.org/10.5194/acp-20-7271-2020, 2020.

680   Stohl, A., Hittenberger, M., and Wotawa, G.: Validation of the lagrangian particle dispersion model FLEXPART against large-scale tracer experiment data, Atmospheric Environment, 32, 4245–4264, https://doi.org/10.1016/S1352-2310(98)00184-8, 1998.

Stohl, A., Forster, C., Frank, A., Seibert, P., and Wotawa, G.: Technical note: The Lagrangian particle dispersion model FLEXPART version 6.2, Atmospheric Chemistry and Physics, 5, 2461–2474, https://doi.org/10.5194/acp-5-2461-2005, 2005.

Stohl, A., Seibert, P., Arduini, J., Eckhardt, S., Fraser, P., Greally, B. R., Lunder, C., Maione, M., Mühle, J., O'Doherty, S., Prinn, R. G.,
685   Reimann, S., Saito, T., Schmidbauer, N., Simmonds, P. G., Vollmer, M. K., Weiss, R. F., and Yokouchi, Y.: An analytical inversion method for determining regional and global emissions of greenhouse gases: Sensitivity studies and application to halocarbons, Atmospheric Chemistry and Physics, 9, 1597–1620, https://doi.org/10.5194/acp-9-1597-2009, 2009.

Stohl, A., Kim, J., Li, S., O'Doherty, S., Yao, B., Yokouchi, Y., and Zhou, L. X.: Hydrochlorofluorocarbon and hydrofluorocarbon emissions in East Asia determined by inverse modeling, Atmospheric Chemistry and Physics, 10, 3545–3560, https://doi.org/10.5194/acp-10-3545-
690   2010, 2010.

Sweeney, C., Karion, A., Wolter, S., Newberger, T., Guenther, D., Higgs, J. A., Andrews, A. E., Lang, P. M., Neff, D., Dlugokencky, E., Miller, J. B., Montzka, S. A., Miller, B. R., Masarie, K. A., Biraud, S. C., Novelli, P. C., Crotwell, M., Crotwell, A. M., Thoning, K., and Tans, P. P.: Seasonal Climatology of CO2 across North America from Aircraft Measurements in the NOAA/ESRL Global Greenhouse Gas Reference Network, Journal of Geophysical Research: Atmospheres, 120, 5155–5190, https://doi.org/10.1002/2014JD022591, 2015.

695   Tarantola, A.: Inverse Problem Theory and Methods for Model Parameter Estimation, pp. 1–67, Society for Industrial and Applied Mathematics, https://doi.org/10.1137/1.9780898717921, 2005.

Thacker, W. C.: Data assimilation with inequality constraints, Ocean Modelling, 16, 264–276, https://doi.org/10.1016/j.ocemod.2006.11.001, 2007.

Thompson, R. L. and Stohl, A.: FLEXINVERT: an atmospheric Bayesian inversion framework for determining surface fluxes of trace species
700   using an optimized grid, Geoscientific Model Development, 7, 2223–2242, https://doi.org/10.5194/gmd-7-2223-2014, 2014.

Thompson, R. L., Stohl, A., Zhou, L. X., Dlugokencky, E., Fukuyama, Y., Tohjima, Y., Kim, S.-Y., Lee, H., Nisbet, E. G., Fisher, R. E., Lowry, D., Weiss, R. F., Prinn, R. G., O'Doherty, S., Young, D., and White, J. W. C.: Methane emissions in East Asia for 2000-2011 estimated using an atmospheric Bayesian inversion, Journal of Geophysical Research: Atmospheres, 120, 4352–4369, https://doi.org/10.1002/2014JD022394, 2015.

705   Trusilova, K., Rödenbeck, C., Gerbig, C., and Heimann, M.: A new coupled system for global-to-regional downscaling of CO 2 concentration estimation, Atmospheric Chemistry and Physics, 10, 3205–3213, https://doi.org/10.5194/acp-10-3205-2010, 2010.

UNFCCC: United Nations Framework Convention on Climate Change, https://di.unfccc.int/time_series, last accessed: 2021-03-10, 2021.

Villani, M., Bergamaschi, P., Krol, M., Meirink, J., and Dentener, F.: Inverse modeling of European CH 4 emissions: sensitivity to the observational network, Atmospheric chemistry and physics, 10, 1249–1267, https://doi.org/10.5194/acp-10-1249-2010, 2010.

710 Vollmer, M. K., Mühle, J., Trudinger, C. M., Rigby, M., Montzka, S. A., Harth, C. M., Miller, B. R., Henne, S., Krummel, P. B., Hall, B. D., Young, D., Kim, J., Arduini, J., Wenger, A., Yao, B., Reimann, S., O'Doherty, S., Maione, M., Etheridge, D. M., Li, S., Verdonik, D. P., Park, S., Dutton, G., Steele, L. P., Lunder, C. R., Rhee, T. S., Hermansen, O., Schmidbauer, N., Wang, R. H. J., Hill, M., Salameh, P. K., Langenfelds, R. L., Zhou, L., Blunier, T., Schwander, J., Elkins, J. W., Butler, J. H., Simmonds, P. G., Weiss, R. F., Prinn, R. G., and Fraser, P. J.: Atmospheric histories and global emissions of halons H-1211 (CBrClF2), H-1301 (CBrF3), and H-2402 (CBrF2CBrF2), Journal of

715 Geophysical Research: Atmospheres, 121, 3663–3686, https://doi.org/10.1002/2015JD024488, 2016.

WDCGG: World Data Centre for Greenhouse Gases, https://gaw.kishou.go.jp/, last accessed: 2022-04-27, 2018.

Weiss, R. F., Ravishankara, A. R., and Newman, P. A.: Huge gaps in detection networks plague emissions monitoring, Nature, 595, 491–493, https://doi.org/10.1038/d41586-021-01967-z, 2021.

World Bank: Electric power consumption, https://data.worldbank.org/indicator/EG.USE.ELEC.KH.PC, last accessed: 2022-04-27, 2021.

720 Yokouchi, Y., Taguchi, S., Saito, T., Tohjima, Y., Tanimoto, H., and Mukai, H.: High frequency measurements of HFCs at a remote site in east Asia and their implications for Chinese emissions, Geophysical Research Letters, 33, https://doi.org/10.1029/2006GL026403, 2006.

Zeng, J., Nakajima, H., Matsunaga, T., Mukai, H., Hiraki, K., and Yokota, Y.: Linking carbon dioxide variability at Hateruma station to East Asia emissions by Bayesian inversion, in: Lagrangian Modeling of the Atmosphere, Geophys. Monograph Series, vol. 200, pp. 163–172, https://doi.org/10.1029/2012GM001245, 2012.

725 Zhao, C., Andrews, A. E., Bianco, L., Eluszkiewicz, J., Hirsch, A., MacDonald, C., Nehrkorn, T., and Fischer, M. L.: Atmospheric Inverse Estimates of Methane Emissions from Central California, Journal of Geophysical Research: Atmospheres, 114, https://doi.org/10.1029/2008JD011671, 2009.